# IOWA STATE UNIVERSITY
**Digital Repository**

2019

# Atomic-level engineering and in-situ spectroscopy studies of metal-organic frameworks in heterogeneous catalysis

Tian Wei Goh
*Iowa State University*

Follow this and additional works at: https://lib.dr.iastate.edu/etd

Part of the Engineering Commons, and the Library and Information Science Commons

## Recommended Citation

**Atomic-level engineering and in-situ spectroscopy studies of metal-organic frameworks in heterogeneous catalysis**

by

**Tian Wei Goh**

A dissertation submitted to the graduate faculty

in partial fulfillment of the requirements for the degree of

DOCTOR OF PHILOSOPHY

Major: Inorganic Chemistry

Program of Study Committee:
Wenyu Huang, Major Professor
Ludovico Cademartiri
Gordon Miller
Aaron Sadow
Levi Stanley

The student author, whose presentation of the scholarship herein was approved by the program of study committee, is solely responsible for the content of this dissertation. The Graduate College will ensure this dissertation is globally accessible and will not permit alterations after a degree is conferred.

Iowa State University
Ames, Iowa
2019

# TABLE OF CONTENTS

# ACKNOWLEDGMENTS

I am forever grateful to Prof Wenyu Huang who inspire me to pursue graduate research in Chemistry. Thank you for being an excellent mentor and providing me with unlimited opportunities to acquire the skills to be a better chemist. I would also like to thank each of committee members Prof. Ludovico Cademartiri, Prof. Gordie Miller, Prof. Aaron Sadow, and Prof. Levi Stanley for all the guidance, helpful discussion, research collaborations and willingness to serve on my committee. I would also like to thank Steve Veysey for giving me the opportunity to learn on using and troubleshooting various instrument in the Chemical Instrumentation Facility. Thank you, Sarah Cady, for all your help on operating the EPR and NMR spectrometer. Thank you, to Lin Zhou, Kewei Sun and Tao Ma for giving me the opportunity to learn various techniques in electron microscopy and providing me with unrestricted access to the electron microscopes in Ames Laboratory.

I am extremely grateful to Prof. Marek Pruski, and Prof. Aaron Rossini for giving me the opportunity to participate in the solid-state NMR project. Thank you to Takeshi Kobayashi, Frédéric Perras, Michael Hanrahan, Amrit Venkatesh and Rick Dorn who I have the pleasure to work with and learn on the fundamentals of solid-state NMR. I would also like to thank Prof. Chia-Kuang (Frank) Tsung and Prof. Feng (Franklin) Tao for all the excellent collaborations, discussion, and pushing my analytical skills limit to characterize many unique nanomaterials. I'd also like to thank the past and current members of Prof. Wenyu Huang for giving me the opportunity to contribute to their excellent research projects. Thanks, to Chaoxian Xiao for being an excellent mentor, and

a role model to me. Thank you to all the wonderful mentees, interns, and undergraduate researchers that I have the pleasure to work with.

Last but not least, I really appreciate the continuous support from my family, my parents, brother, and sister for letting me pursue my life choices.

# ABSTRACT

Metal-organic frameworks (MOFs) have shown promise as an efficient platform in various applications especially in the field of heterogeneous catalysis. The inherent properties of MOFs such as high surface area and porosity, thermal and chemical stability while remaining as a highly crystalline solid with molecular precision tunability allow us to perform many fundamental studies to resolve structural-property relationship in the application in heterogeneous catalysis. In this thesis, we discussed the atomic-level engineering approach to design MOFs to be an active catalyst for application in visible light photocatalysis and using MOFs as a host to stabilize monodisperse ultrafine nanoclusters. The high crystallinity of the MOF further provides a uniform local chemical environment that allows us to resolve the structure to various advance spectroscopy techniques such as in-situ X-ray Absorption Spectroscopy (XAS), diffuse reflectance infrared Fourier-transform spectroscopy (DRIFTS), and solid-state nuclear magnetic resonance (ssNMR) spectroscopy.

## CHAPTER 1. INTRODUCTION

### 1.1 General Introduction

Metal-organic frameworks (MOFs) are crystalline porous solid-state materials that are assembled from the combination of metal ions, or metal-oxo clusters with organic ligands. The first stable MOF that exhibit permanent porosity was isolated by Omar Yaghi in 1999, which is assembled from a $Zn_4O(CO_2)_6$ secondary building units (SBU) linked by benzenedicarboxylate organic ligands, MOF-5 (Figure 1).[1] The concept of rational assembling of molecular SBU units with organic ligands through metal-organic coordination bonds to create an extended crystalline framework is known as reticular chemistry.[2-3] Through the concept of reticular chemistry, thousands of highly porous crystalline solid materials have been prepared by varying the length, functional groups, and geometry of the organic ligands coupled with SBU consist of different transition metals.[4-7]
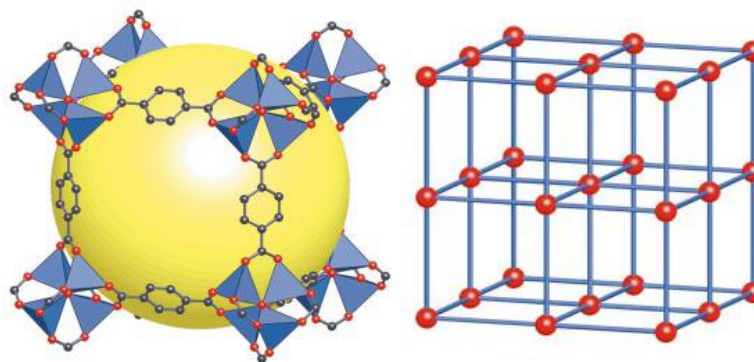


Figure 1. MOF-5 shown as $ZnO_4$ tetrahedra (blue polyhedra) joined by benzenedicarboxylate linkers (O, red and C, black) to give an extended 3D cubic framework with interconnected pores of 8 Å aperture width and 12 Å pore (yellow sphere) diameter. Reproduced from reference.[3]

In the past twenty years, MOFs has gained tremendous attention from researchers in various fields as shown by the increasing of publication records (Figure 2). The ability to rationally designed the structure, functionality, and properties of this crystalline porous solids has resulted in the exploration of its applications in gas storage, separation, sensing, drug carriers, catalysis and most recently water capture.[5, 7-15] Among the enormous family of metal-organic frameworks, zirconium-based MOFs was one of the most studied structure since the isolation of the first MOFs assembled from the $Zr_6O_4(OH)_4(CO_2)_{12}$ building block and dicarboxylate organic ligands by the Lillerud's group from University of Oslo in 2008.[16] The first generation of Zr-based MOF known as the UiO family exhibit unprecedented thermal and chemical stability compared to other reported MOFs based on different transition metals SBUs such as Fe, Cu, and Al.[4, 16-20] The stability of the Zr-based MOFs was proposed to stem from multiple factors such as the high oxidation state of the SBUs, the reduction potential and ionic radius of the $Zr^{4+}$ cations, the metal-ligand coordination geometry, and hydrophobicity of the pores.[18, 21] A major factor in the stability of the Zr-based MOFs is due to the high charge density and bond polarization between the carboxylates' oxygen atoms with the oxophilic nature of $Zr^{4+}$ in the $Zr_6O_4(OH)_4(CO_2)_{12}$.[4, 22] This bond polarization effect of hard/soft acid/base was proposed by Ralph Pearson in 1963.[23]
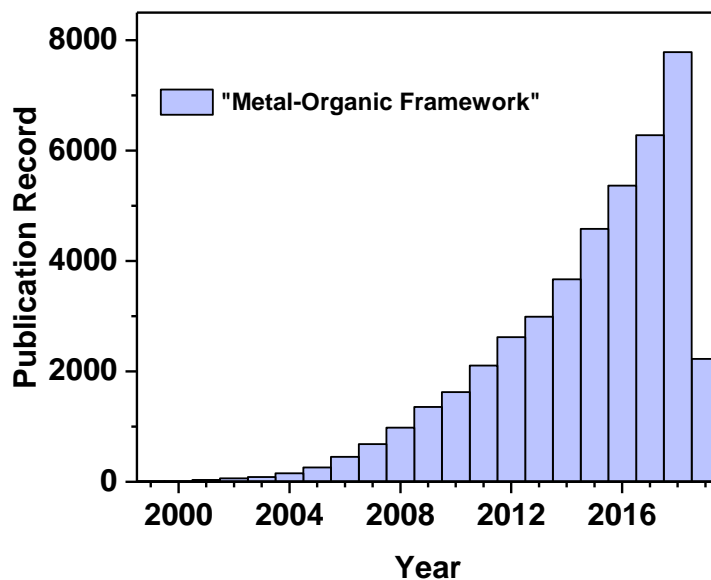
Figure 2. Year-by-year increases of publication record of the metal-organic framework in the past twenty years according to the Web of Science database (accessed on March 28th, 2019).

     The application of MOFs as heterogeneous catalysts has been widely investigated by many research groups in recent years.[14-15, 24-26] Early example of MOF as a heterogeneous catalyst was pioneered by Fujita and co-worker using a cadmium-bipyridine clathrate structure to catalyze the cyanosilylation of aldehydes. Although the solid catalyst has poor catalytic performance and stability, the uniform cubic pore of the metal-organic clathrates provides a shape selectivity in the cyanosilylation of methyl aldehydes.[27] Over the years, extensive research has been done in optimizing MOFs as heterogeneous catalysts for different organic transformation. Zr-based MOFs has emerged as an ideal candidate for the application in heterogeneous catalysis due to its robustness, high surface area, uniform pore size, and the ease of functionality.[4] Zr-based MOFs with *fcu* or *bcu* network topology was generally prepared by solvothermal synthesis using equivalent amount of dicarboxylate ligand and $Zr^{4+}$ salt dissolved in coordinating solvent such as dimethylformamide (DMF), and incubated in at 120 °C for 24

hours (Scheme 1). The resulting solids were further isolated and washed with copious amount of reaction solvent to remove any unreacted starting materials. The solid was further undergoes solvent exchange with a low boiling solvents such as acetone, or methylene chloride in order to preserve the porosity upon complete removal of the solvent guest molecules.

$$6\,H_2BDC + 6\,ZrCl_4 \xrightarrow[120\ °C\ /\ 24\ h]{DMF/H_2O} Zr_6O_4(OH)_4(BDC)_6 + 24\,HCl$$
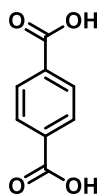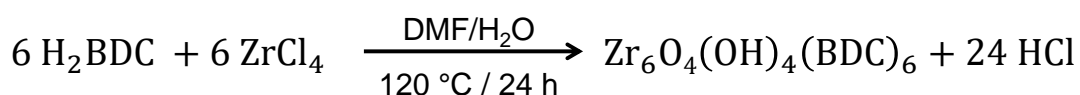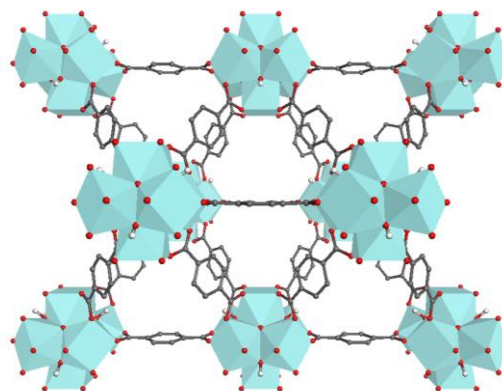


Benzenedicarboxylic acid
(H$_2$BDC)

Cubic *Fm-3m*    Surface area: 1187 m$^2$/g
a = 20.7004(2) Å    Pore diameter: 6.0 Å
V = 8870.3(2) Å$^3$

Scheme 1. General synthesis procedure of Zr-based MOF (UiO-66). Zr$_6$O$_4$(OH$_4$) is shown as cyan polyhedral joined by benzenedicarboxylate ligands (O, red and C, black) to give an extended fcu framework with a triangular pore diameter of 6 Å.

In general, there are two major approaches in incorporating catalytic active sites into the MOF, i) incorporation of catalytic active sites into the MOFs scaffold through the SBU and organic linkers as shown in Figure 3, or ii) encapsulation or immobilizing homogeneous catalyst or catalytic active nanostructures into/onto the MOFs. Through the first approach, the catalytic active sites can be generated in-situ or de novo during the synthesis of the MOFs or

through post-synthetic modifications[28] of the as-synthesized MOF structure. Three different types of catalytic active sites can be generated from the MOF scaffold as shown in Figure 3.

In the Type I catalyst, the active sites involve using the SBU typically an undercoordinated metal-nodes which can act as a Lewis acid or Bronsted acid for acid catalyzed reaction. The undercoordinated Zr-oxo cluster has been used extensively as both Lewis and Bronsted acid sites to catalyze acetalizations of aldehyde, cyclization of citronellal, and isomerization of alkenes.[29-33] Besides, the Zr-oxo nodes can also act as the active sites in photocatalytic oxidation reaction through ligand-to-metal charge transfer (LMCT) upon excitation with a light source.[34-39] By varying the functionalities on the dicarboxylate ligands that bridge the Zr-oxo clusters, the band gap of the MOF can be tuned, thus allowing the absorption of visible light and broader light spectrum for visible light photocatalysis. The first example of using mixed dicarboxylate linker in MOF construction for visible light photo oxidation of alcohol was further elaborated in **Chapter 2** of this thesis.[40]
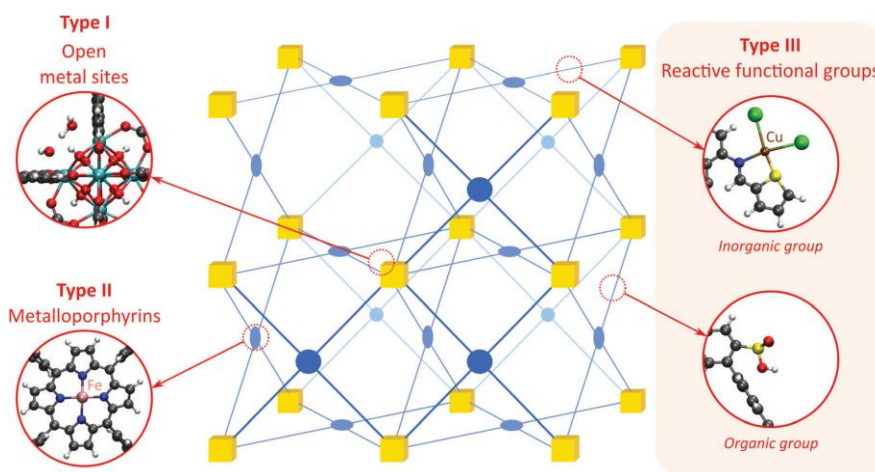


Figure 3. Classification of the different positions in porous framework materials where catalytic reactions can take place. The inorganic nodes are indicated with yellow cubes,

whereas the structure-defining ligands are indicated in blue. Possible terminating ligands at the inorganic nodes are not indicated, as they do not contribute to the topology of the material. Reproduced from reference.[15]

Type II catalysts utilize the organic ligands, or the functional groups on the ligands to stabilize the catalytic active transition metal, while Type III uses the functional group itself as the catalytic active sites. Besides these three types of heterogeneous catalysts derived from the MOF scaffold, MOF can also be used as a host or support for encapsulation or active catalysts, such as noble metal nanoparticles, intermetallic nanoparticles, bulky homogeneous catalysts, and solid acid catalysts. Nanocrystalline Zr-MOF with high surface area, with a uniform pore size act as an excellent template and support to prepare monodispersed ultrasmall nanoparticles.

In our group, we have developed the method of using amino group functionalized benzenedicarboxylate as the linker in the construction Zr-based MOF. The ligand which consists of a free amino group is able to stabilize the transition metal complexes such as $PtCl_4^{2-}$ through ligand exchange. The immobilization of $PtCl_4^{2-}$ complexes into the UiO-66-$NH_2$ was monitored in-situ using X-ray absorption spectroscopy which was conducted at Advanced Photon Source, Argonne National Laboratory.[41] Upon immobilization of the $PtCl_4^{2-}$ into the cavity of the MOFs, the Pt@MOFs was isolated and subjected to reduction at elevated temperature in $H_2$ atmosphere as depicted in Scheme 2. The reduction of the Pt complexes led to the formation of monodispersed 1.2 nm Pt nanoparticles. The monodispersity was due to the space confinement by the uniform pore size of the nanocrystalline MOFs. The selective incorporation of $Pt^{2+}$ metal complexes into the MOF and the formation of Pt nanoparticles was

also extensively investigated using solid-state nuclear magnetic resonance spectroscopy (ssNMR) in collaboration with Prof. Marek Pruski in Ames Laboratory.[42-44] Using the space confinement effect from the MOF's pore, we further use this methodology to prepare bimetallic nanoparticles through step-wise impregnation which will be discussed in further in **Chapter 3**.
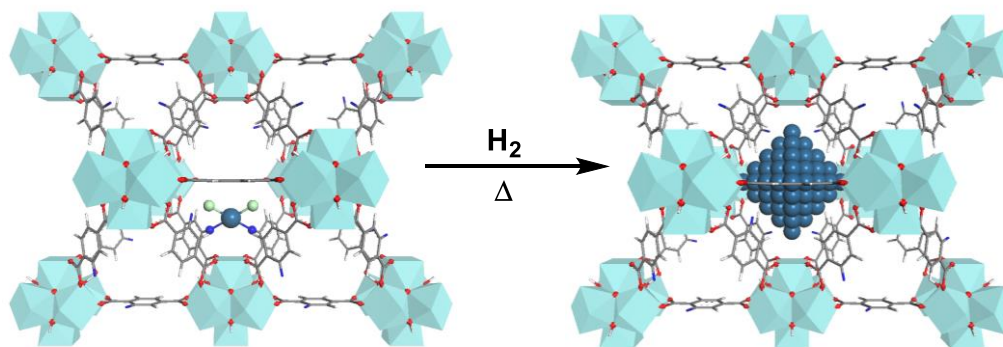


Scheme 2. Immobilization of $PtCl_4^{2-}$ complexes in UiO-66-NH$_2$ and subsequent gas phase reduction by H$_2$ gas to prepare 1.2 nm Pt nanoparticles.

Driven by the advancement of characterization tools and affordable computing power for simulation, material characterization has been able to reach the atomic-level resolution.[45] This has promoted the exploration and development of atomically dispersed single-atom catalyst (SAC). Isolated single-atom supported on high surface area, and robust materials such as metal oxides, zeolites, metal-organic frameworks (MOFs), and carbon-based materials presents a maximum atomic efficiency and new catalytic properties due to the unique electronic properties.[46-50] In **Chapter 4**, we have demonstrated the use of in-situ and operando diffuse reflectance infrared spectroscopy (DRIFTS) to resolve the thermally stable isolated Pt single atom in the MOF scaffold.

## 1.2 References

1.      Li, H.; Eddaoudi, M.; O'Keeffe, M.; Yaghi, O. M., Design and synthesis of an exceptionally stable and highly porous metal-organic framework. *Nature* **1999,** *402* (6759), 276-279.

2.      O'Keeffe, M.; Peskov, M. A.; Ramsden, S. J.; Yaghi, O. M., The Reticular Chemistry Structure Resource (RCSR) Database of, and Symbols for, Crystal Nets. *Acc. Chem. Res.* **2008,** *41* (12), 1782-1789.

3.      Yaghi, O. M.; O'Keeffe, M.; Ockwig, N. W.; Chae, H. K.; Eddaoudi, M.; Kim, J., Reticular synthesis and the design of new materials. *Nature* **2003,** *423* (6941), 705-714.

4.      Bai, Y.; Dou, Y.; Xie, L.-H.; Rutledge, W.; Li, J.-R.; Zhou, H.-C., Zr-based metal-organic frameworks: design, synthesis, structure, and applications. *Chem. Soc. Rev.* **2016,** *45* (8), 2327-2367.

5.      Bosch, M.; Yuan, S.; Rutledge, W.; Zhou, H.-C., Stepwise Synthesis of Metal–Organic Frameworks. *Acc. Chem. Res.* **2017,** *50* (4), 857-865.

6.      Eddaoudi, M.; Kim, J.; Rosi, N.; Vodak, D.; Wachter, J.; O'Keeffe, M.; Yaghi, O. M., Systematic Design of Pore Size and Functionality in Isoreticular MOFs and Their Application in Methane Storage. *Science* **2002,** *295* (5554), 469-472.

7.      Rungtaweevoranit, B.; Diercks, C. S.; Kalmutzki, M. J.; Yaghi, Omar M., Spiers Memorial Lecture: Progress and prospects of reticular chemistry. *Faraday Discuss.* **2017,** *201* (0), 9-45.

8.      Lee, J.; Farha, O. K.; Roberts, J.; Scheidt, K. A.; Nguyen, S. T.; Hupp, J. T., Metal-organic framework materials as catalysts. *Chem. Soc. Rev.* **2009,** *38* (5), 1450-1459.

9.      Li, J.-R.; Kuppler, R. J.; Zhou, H.-C., Selective gas adsorption and separation in metal-organic frameworks. *Chem. Soc. Rev.* **2009,** *38* (5), 1477-1504.

10.     Liu, J.; Thallapally, P. K.; McGrail, B. P.; Brown, D. R.; Liu, J., Progress in adsorption-based $CO_2$ capture by metal-organic frameworks. *Chem. Soc. Rev.* **2012,** *41* (6), 2308-2322.

11.     Shekhah, O.; Liu, J.; Fischer, R. A.; Woll, C., MOF thin films: existing and future applications. *Chem. Soc. Rev.* **2011,** *40* (2), 1081-1106.

12.     Smith, B. M., Catalytic methods for the destruction of chemical warfare agents under ambient conditions. *Chem. Soc. Rev.* **2008,** *37* (3), 470-478.

13.     Zhang, T.; Lin, W., Metal-organic frameworks for artificial photosynthesis and photocatalysis. *Chem. Soc. Rev.* **2014**.

14.     Gascon, J.; Corma, A.; Kapteijn, F.; Llabrés i Xamena, F. X., Metal Organic Framework Catalysis: Quo vadis? *ACS Catal.* **2013**, 361-378.

15.     Rogge, S. M. J.; Bavykina, A.; Hajek, J.; Garcia, H.; Olivos-Suarez, A. I.; Sepúlveda-Escribano, A.; Vimont, A.; Clet, G.; Bazin, P.; Kapteijn, F.; Daturi, M.; Ramos-Fernandez, E. V.; Llabrés i Xamena, F. X.; Van Speybroeck, V.; Gascon, J., Metal–organic and covalent organic frameworks as single-site catalysts. *Chem. Soc. Rev.* **2017,** *46* (11), 3134-3184.

16.     Cavka, J. H.; Jakobsen, S.; Olsbye, U.; Guillou, N.; Lamberti, C.; Bordiga, S.; Lillerud, K. P., A New Zirconium Inorganic Building Brick Forming Metal Organic Frameworks with Exceptional Stability. *J. Am. Chem. Soc.* **2008,** *130* (42), 13850-13851.

17.     Kandiah, M.; Nilsen, M. H.; Usseglio, S.; Jakobsen, S.; Olsbye, U.; Tilset, M.; Larabi, C.; Quadrelli, E. A.; Bonino, F.; Lillerud, K. P., Synthesis and Stability of Tagged UiO-66 Zr-MOFs. *Chem. Mater.* **2010,** *22* (24), 6632-6640.

18.     DeCoste, J. B.; Peterson, G. W.; Jasuja, H.; Glover, T. G.; Huang, Y.-g.; Walton, K. S., Stability and degradation mechanisms of metal–organic frameworks containing the Zr6O4(OH)4 secondary building unit. *Journal of Materials Chemistry A* **2013,** *1* (18), 5642-5650.

19.     Valenzano, L.; Civalleri, B.; Chavan, S.; Bordiga, S.; Nilsen, M. H.; Jakobsen, S.; Lillerud, K. P.; Lamberti, C., Disclosing the Complex Structure of UiO-66 Metal Organic Framework: A Synergic Combination of Experiment and Theory. *Chem. Mater.* **2011,** *23* (7), 1700-1718.

20.     Devic, T.; Serre, C., High valence 3p and transition metal based MOFs. *Chem. Soc. Rev.* **2014,** *43* (16), 6097-6115.

21.     Burtch, N. C.; Jasuja, H.; Walton, K. S., Water Stability and Adsorption in Metal–Organic Frameworks. *Chem. Rev. (Washington, DC, U. S.)* **2014,** *114* (20), 10575-10612.

22.	Zhang, M.; Chen, Y.-P.; Bosch, M.; Gentle III, T.; Wang, K.; Feng, D.; Wang, Z. U.; Zhou, H.-C., Symmetry-Guided Synthesis of Highly Porous Metal–Organic Frameworks with Fluorite Topology. *Angew. Chem. Int. Ed.* **2014,** *53* (3), 815-818.

23.	Pearson, R. G., Hard and Soft Acids and Bases. *J. Am. Chem. Soc.* **1963,** *85* (22), 3533-3539.

24.	Corma, A.; García, H.; Llabrés i Xamena, F. X., Engineering Metal Organic Frameworks for Heterogeneous Catalysis. *Chem. Rev. (Washington, DC, U. S.)* **2010,** *110* (8), 4606-4655.

25.	Dhakshinamoorthy, A.; Alvaro, M.; Corma, A.; Garcia, H., Delineating similarities and dissimilarities in the use of metal organic frameworks and zeolites as heterogeneous catalysts for organic reactions. *Dalton Trans.* **2011,** *40* (24), 6344-6360.

26.	Farrusseng, D.; Aguado, S.; Pinel, C., Metal–Organic Frameworks: Opportunities for Catalysis. *Angew. Chem. Int. Ed.* **2009,** *48* (41), 7502-7513.

27.	Fujita, M.; Kwon, Y. J.; Washizu, S.; Ogura, K., Preparation, Clathration Ability, and Catalysis of a Two-Dimensional Square Network Material Composed of Cadmium(II) and 4,4'-Bipyridine. *J. Am. Chem. Soc.* **1994,** *116* (3), 1151-1152.

28.	Wang, Z.; Cohen, S. M., Postsynthetic modification of metal-organic frameworks. *Chem. Soc. Rev.* **2009,** *38* (5), 1315-1329.

29.	Vermoortele, F.; Bueken, B.; Le Bars, G.; Van de Voorde, B.; Vandichel, M.; Houthoofd, K.; Vimont, A.; Daturi, M.; Waroquier, M.; Van Speybroeck, V.; Kirschhock, C.; De Vos, D. E., Synthesis Modulation as a Tool To Increase the Catalytic Activity of Metal–Organic Frameworks: The Unique Case of UiO-66(Zr). *J. Am. Chem. Soc.* **2013,** *135* (31), 11465-11468.

30.	Li, X. L.; Guo, Z. Y.; Xiao, C. X.; Goh, T. W.; Tesfagaber, D.; Huang, W. Y., Tandem Catalysis by Palladium Nanoclusters Encapsulated in Metal-Organic Frameworks. *ACS Catal.* **2014,** *4* (10), 3490-3497.

31.	Li, X. L.; Goh, T. W.; Li, L.; Xiao, C. X.; Guo, Z. Y.; Zeng, X. C.; Huang, W. Y., Controlling Catalytic Properties of Pd Nanoclusters through Their Chemical Environment at the Atomic Level Using Isoreticular Metal-Organic Frameworks. *ACS Catal.* **2016,** *6* (6), 3461-3468.

32.    Jiang, J.; Gándara, F.; Zhang, Y.-B.; Na, K.; Yaghi, O. M.; Klemperer, W. G., Superacidity in Sulfated Metal–Organic Framework-808. *J. Am. Chem. Soc.* **2014,** *136* (37), 12844-12847.

33.    Trickett, C. A.; Osborn Popp, T. M.; Su, J.; Yan, C.; Weisberg, J.; Huq, A.; Urban, P.; Jiang, J.; Kalmutzki, M. J.; Liu, Q.; Baek, J.; Head-Gordon, M. P.; Somorjai, G. A.; Reimer, J. A.; Yaghi, O. M., Identification of the strong Brønsted acid site in a metal–organic framework solid acid catalyst. *Nature Chem.* **2018**.

34.    Nasalevich, M. A.; Goesten, M. G.; Savenije, T. J.; Kapteijn, F.; Gascon, J., Enhancing optical absorption of metal-organic frameworks for improved visible light photocatalysis. *Chem. Commun.* **2013,** *49* (90), 10575-10577.

35.    Gascon, J.; Hernández-Alonso, M. D.; Almeida, A. R.; van Klink, G. P. M.; Kapteijn, F.; Mul, G., Isoreticular MOFs as Efficient Photocatalysts with Tunable Band Gap: An Operando FTIR Study of the Photoinduced Oxidation of Propylene. *ChemSusChem* **2008,** *1* (12), 981-983.

36.    Dhakshinamoorthy, A.; Li, Z.; Garcia, H., Catalysis and photocatalysis by metal organic frameworks. *Chem. Soc. Rev.* **2018,** *47* (22), 8134-8172.

37.    Wang, S.; Wang, X., Multifunctional Metal–Organic Frameworks for Photocatalysis. *Small* **2015,** *11* (26), 3097-3112.

38.    Zhang, T.; Lin, W., Metal–organic frameworks for artificial photosynthesis and photocatalysis. *Chem. Soc. Rev.* **2014,** *43* (16), 5982-5993.

39.    Nasalevich, M. A.; van der Veen, M.; Kapteijn, F.; Gascon, J., Metal–organic frameworks as heterogeneous photocatalysts: advantages and challenges. *CrystEngComm* **2014,** *16* (23), 4919-4926.

40.    Goh, T. W.; Xiao, C.; Maligal-Ganesh, R. V.; Li, X.; Huang, W., Utilizing mixed-linker zirconium based metal-organic frameworks to enhance the visible light photocatalytic oxidation of alcohol. *Chem. Eng. Sci.* **2015,** *124*, 45-51.

41.    Xiao, C.; Goh, T. W.; Brashler, K.; Pei, Y.; Guo, Z.; Huang, W., In situ X-ray absorption spectroscopy studies of kinetic interaction between platinum(II) ions and UiO-66 series metal-organic frameworks. *J. Phys. Chem. B* **2014,** *118* (49), 14168-76.

42.     Guo, Z.; Kobayashi, T.; Wang, L. L.; Goh, T. W.; Xiao, C.; Caporini, M. A.; Rosay, M.; Johnson, D. D.; Pruski, M.; Huang, W., Selective host-guest interaction between metal ions and metal-organic frameworks using dynamic nuclear polarization enhanced solid-state NMR spectroscopy. *Chemistry* **2014,** *20* (49), 16308-13.

43.     Kobayashi, T.; Perras, F. A.; Goh, T. W.; Metz, T. L.; Huang, W.; Pruski, M., DNP-Enhanced Ultrawideline Solid-State NMR Spectroscopy: Studies of Platinum in Metal-Organic Frameworks. *J Phys Chem Lett* **2016,** *7* (13), 2322-7.

44.     Perras, F. A.; Venkatesh, A.; Hanrahan, M. P.; Goh, T. W.; Huang, W.; Rossini, A. J.; Pruski, M., Indirect detection of infinite-speed MAS solid-state NMR spectra. *J Magn Reson* **2017,** *276*, 95-102.

45.     Liu, J., Aberration-corrected scanning transmission electron microscopy in single-atom catalysis: Probing the catalytically active centers. *Chin. J. Catal.* **2017,** *38* (9), 1460-1472.

46.     Drake, T.; Ji, P.; Lin, W., Site Isolation in Metal–Organic Frameworks Enables Novel Transition Metal Catalysis. *Acc. Chem. Res.* **2018**.

47.     Liang, Z.; Qu, C.; Xia, D.; Zou, R.; Xu, Q., Atomically Dispersed Metal Sites in MOF-Based Materials for Electrocatalytic and Photocatalytic Energy Conversion. *Angew. Chem. Int. Ed.* **2018,** *57* (31), 9604-9633.

48.     Yamashita, H.; Mori, K.; Kuwahara, Y.; Kamegawa, T.; Wen, M.; Verma, P.; Che, M., Single-site and nano-confined photocatalysts designed in porous materials for environmental uses and solar fuels. *Chem. Soc. Rev.* **2018,** *47* (22), 8072-8096.

49.     Yang, X.-F.; Wang, A.; Qiao, B.; Li, J.; Liu, J.; Zhang, T., Single-Atom Catalysts: A New Frontier in Heterogeneous Catalysis. *Acc. Chem. Res.* **2013,** *46* (8), 1740-1748.

50.     Wang, A.; Li, J.; Zhang, T., Heterogeneous single-atom catalysis. *Nature Reviews Chemistry* **2018,** *2* (6), 65-81.

# CHAPTER 2.   UTILIZING MIXED-LINKER ZIRCONIUM BASED METAL-ORGANIC FRAMEWORK TO ENHANCE THE VISIBLE LIGHT PHOTOCATALYTIC OXIDATION OF ALCOHOL

Tian Wei Goh, Chaoxian Xiao, Raghu V. Maligal-Ganesh, Xinle Li, Prof. Wenyu

Huang

## 2.1 Abstract

A series of mixed-linker zirconium-based metal-organic frameworks (Zr-MOFs) have been synthesized in one-pot reactions. The Zr-MOFs, containing 2-amino-1,4-benzenedicarboxylate ($NH_2$-BDC) as the primary linker and 2-X-1,4-bezenedicarboxylate (X-BDC, X = H, F, Cl, Br) as a secondary linker, have been used as visible light photocatalysts. The incorporation of multi-functional groups into the catalysts was characterized by PXRD, STEM, NMR, $N_2$ physisorption diffuse reflectance FTIR, and diffuse reflectance UV-Vis. The effects of different linkers on the photocatalytic property of the Zr-MOFs were evaluated in the oxidation of benzyl alcohol. The photocatalytic oxidation reaction was performed using a 26 W helical bulb as the visible light source, and the temperature of the reaction was kept at 80 °C. The Zr-MOF containing mixed $NH_2$-BDC and F-BDC linkers gives five times more conversion in the oxidation of benzyl alcohol compared to the Zr-MOF made of mixed $NH_2$-BDC and H-BDC linkers. We only observed partial oxidation product, benzaldehyde, from the photocatalytic oxidation reaction.

## 2.2 Introduction

Since the discovery of ultraviolet (UV) light-irradiated, photocatalytically active $TiO_2$ by Honda and Fujishima in 1972,[1] immense efforts have been directed to improve the efficiency of this semiconductor.[2] This led to a spurt of research towards utilizing light as an effective source of energy for many important chemical transformations. By applying molecular orbital theory, significant advances have been made in the design of these photocatalysts owing to an improved understanding of the utilization of light energy by molecules.[3] Traditional semiconductors, quantum dots,[4] and supramolecular ensembles[5] have also been engineered to efficiently execute photocatalytic reactions. A new class of materials, a hybridized organic-inorganic structural motif known as metal-organic frameworks (MOFs) has emerged as an interesting multi-purpose platform. MOFs have found considerable applications in gas storage,[6] heterogeneous catalysis,[7,8] separations,[9] drug delivery,[10] and chemical sensing.[11] Interestingly, due to the inherent ability to control the functionality of the organic linkers and the inorganic secondary building units during their synthesis,[12] these materials have shown considerable promise for photocatalysis.

Application of MOFs in photocatalysis was first rationalized in the MOF-5 system due to its semiconductivity.[13,14] However, MOF-5 is only active as a catalytic system upon UV light irradiation. To tune the band gap of MOFs to absorb visible light, Fu et al.[15] and other groups[16,17] modified the type of organic bridging linkers and produced visible light active catalysts. However, the catalytically active sites that reside at the inorganic building blocks of these MOFs yield relatively low activity.[18] In comparison, MOF-based photocatalysts synthesized by Lin et al. through linker coordination with redox metal

complexes show significantly enhanced photocatalytic activity in water oxidation, $CO_2$ reduction, and organic transformations.[19]

We hypothesized that incorporating different linkers of appropriate functionalities into a single framework could affect its catalytic property which provides a new opportunity for designing improved catalysts. In literature, the incorporation of different functionalized linkers into a single MOF has been demonstrated by Burrows and coworkers through post-synthetic modification (PSM).[20] Starting with aldehyde-functionalized MOF-5, comprised of $ZnO_4$ clusters connected by aldehyde-functionalized benzenedicarboxylate linkers, Burrows intended to chemically modify the aldehyde group to other useful groups. However, the aldehyde group was only modified partially, resulting in a mixed-linker MOF system. Using a bottom-up approach, Deng and co-workers,[21] incorporated up to six linkers with different functional groups into MOF-5. This MOF was synthesized by a one-pot synthesis approach, where the different linkers were added at the beginning of the synthesis. Besides MOF-5 system, Marx and coworkers introduced mixed linkers into MIL-53(Al).[22] Lin's group produced mixed-linker MIL-101(Fe) for drug delivery applications.[23]

In this report, we synthesized task-specific mixed linker Zr-MOFs using bottom-up approach in one-pot, aiming to improved activity in visible light photocatalytic reactions. We utilized 2-amino-1,4-benzenedicarboxylic acid ($NH_2$-BDC) as a primary linker to shift the absorption wavelength of the parent UiO-66 which comprise of of $Zr_6O_4(OH)_4$ clusters and 1,4-benzenedicarboxylate (BDC) linker[24] to the visible light regime, and a secondary linker, 2-X-1,4-benzenedicarboxylic acid (X-BDC, where X = H, F, Cl, Br) was incorporated in the

same MOF to adjust the local environment and electronic properties around the active sites and thus their activity. Their catalytic performance was evaluated their in the visible light photocatalytic oxidation of benzyl alcohol. The as-synthesized mixed-linker UiO-66 MOFs containing halogen functional groups showed enhanced catalytic activity compared to the UiO-66-NH$_2$ and UiO-66-NH$_2$-H MOFs.

## 2.3 Experimental Section

Anhydrous zirconium tetrachloride (ZrCl$_4$, 98%), and 2-amino-1,4-benzenedicarboxylic acid were purchased from Acros Organics. 2-bromo-1,4-benzendicarboxylic acid and was purchased from Alfa Aesar and benzenedicarboxylic acid was purchased from Sigma Aldrich. All chemicals were used without further purification. 2-chloro-1,4-benzenedicarboxylic, 2-fluoro-1,4-benzenedicarboxylic acid, and 2-iodo-1,4-benzenedicarboxylic acid were synthesized according to a reported procedure in literature.[25,26]

For the synthesis of 2-iodo-1,4-benzenedicarboxylic acid and 2-fluoro-1,4-benzenedicarboxylic acid, the respective functionalized dimethyl terephthalate was used. In general, 0.5 g (2.36 mmol) of dimethyl-2-fluoroterephthalate was dissolved in 20 mL of aqueous sodium hydroxide (1.0 M aqueous NaOH, 1.0 M) at 353 K for 30 minutes with continuous stirring. After 30 minutes, the clear solution was cooled down to room temperature. Concentrated hydrochloric acid (HCl, assay 37%) were added dropwise to the solution while stirring until the pH reaches 1. The resultant white precipitate was recovered by vacuum filtration and wash with copious amount of water to remove the excess acid. The white powder was vacuum dried overnight at room temperature.

For the synthesis of 2-chloro-1,4-benzenedicarboxylic acid, 0.5 g (3.25 mmol) and 1.6 g (9.8 mmol) were dissolved in 20 mL aqueous potassium hydroxide solution (KOH, 2 M). The solution was set to refluxed overnight. The solution was allowed to cool to room temperature and acidified with concentrated hydrochloric acid to pH 1. The precipitate was collected by vacuum filtration and rinse with copious amount of water. The precipitate was dried in vacuum at room temperature to obtained 2-chloro-1,4-benzenedicarboxylic acid.

UiO-66-NH$_2$ was synthesized according to a process reported in literature.[27] In a typical synthesis, 1.7 mmol of zirconium tetrachloride (ZrCl$_4$) was dissolved in 100 mL of dimethylformamide (DMF) in a Teflon PFA wide mouth jar. An equimolar amount of the linker, 2-amino-1,4-benzenedicarboxylic acid (1.7 mmol), was dissolved into the clear solution with the aid of sonication for about 5 minutes. The tightly capped Teflon jar was then transferred into a 120 °C pre-heated oven. The Teflon jar was maintained under static conditions for 24 hours. After 24 hours, the suspension was cooled to room temperature and the precipitate was isolated by centrifugation at 8000 rpm for 15 minutes. The isolated precipitate was washed with 40 mL DMF thrice to remove any unreacted substrates. The precipitate was further washed with methanol to allow the exchange of DMF trapped in the framework with a lower boiling point solvent. During each wash, the suspension was kept at room temperature for 12 hours before being centrifuged. Finally, the precipitate was dried at 150 °C under dynamic vacuum overnight to remove the trapped solvent.

For the synthesis of mixed-linker Zr-MOFs (Scheme 1), 1.7 mmol of zirconium tetrachloride was dissolved in 100 mL DMF in a Teflon PFA wide mouth jar. The primary linker 2-amino-1,4-benzenedicarboxylic acid (0.85 mmol) and the second organic linker 2-X-1,4-benzendicarboxylic acid (0.85 mmol, X = H, F, Cl, Br) were dissolved into the solution by sonication. The Teflon jar was sealed and transferred into a 120 °C preheated oven. After 24 hours, the precipitate was isolated, purified and dried following the same procedure used for UiO-66-NH$_2$. The as-synthesized mixed-linker UiO-66 MOFs were denoted as UiO-66-NH$_2$-X (X = H, F, Cl, Br).
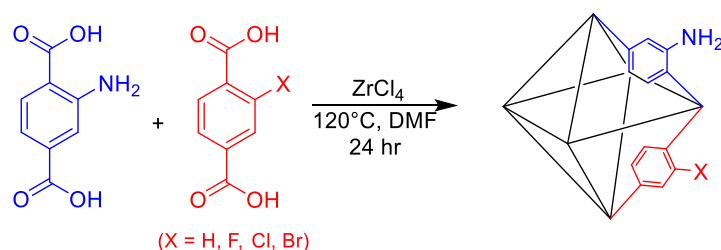


Scheme 1. Synthesis of the mixed-linker Zr-MOFs. Equimolar quantities of primary linker 2-amino-1,4-benzenedicarboxylic acid and secondary linker 2-X-benzene-1,4-dicarboxylic acid (X = H, F, Cl, Br).

## 2.4 Material Characterization

The powder X-ray diffraction (PXRD) patterns were collected at room temperature using a STOE Stadi P powder diffractometer equipped with an image plate and a Cu K$_\alpha$ radiation source (40 kV, 40 mA, λ=1.5405 Å).

For nuclear magnetic resonance (NMR) characterization, about 10 mg of catalyst was digested in 580 µL of DMSO-d$_6$ and 20 µL of HF. After complete dissolution of the catalyst

by sonication, the solution was used to collect a ^{1}H NMR spectrum. ^{1}H NMR spectra were recorded on a Bruker DRX 400 spectrometer at 400.39 MHz.

The size and morphology of the Zr-MOF was investigated using scanning transmission electron microscopy (STEM). Energy-dispersive X-ray (EDX) analysis was used to identify the elements present in the mixed linkers in the Zr-MOF crystal. Scanning transmission electron microscopy (STEM) images was recorded on a Tecnai $G^2$ F20 electron microscope equipped with an EDX detector (Oxford INCA EDS).

Pore volume and surface area measurements using high purity nitrogen were performed using Micromeritics 3Flex Surface Characterization Analyzer. Prior to nitrogen adsorption and desorption measurements, the catalysts were degassed at 423 K for 6 hours. All nitrogen adsorption and desorption was measured at 77 K. Surface areas were determined by the Brunauer-Emmett-Teller (BET) equation in the range between 0.01 to 0.1 relative pressure so that the value of the y-intercept is positive.[28]

Diffuse reflectance infrared Fourier transform spectroscopy (DRIFTS) measurements were performed using Agilent Cary 670 FTIR equipped with a linearized Mercury-Cadmium-Telluride (MCT) detector, a Harrick diffuse reflectance accessory, and a Praying Mantis high temperature reaction chamber. Zr-MOFs were packed in the sample cup, followed by an activation process under high vacuum ($10^{-6}$ torr) at 200 °C for 1 hour to remove any absorbed water. Heating for a longer time does not show any further changes in the IR spectrum. After the sample was cooled down to room temperature, the spectra were recorded at 1 cm$^{-1}$ resolution within the range of 4000–700 cm$^{-1}$. Kubelka–Munk correction was applied to generate the spectra for qualitative analysis. UV-Visible absorbance was measured using a Stellar Solid Diffuse-Reflectance Probe.

## 2.5 Catalytic performance test

The reaction was carried out in a sealed 6-dram glass vial (22.2 mL) with a magnetic stirrer. In a typical reaction, 0.10 mmol of catalyst (based on Zr content) was evacuated at 150 °C under vacuum to remove any absorbed species. The vial was then saturated with $O_2$ and 3 mL of toluene was injected into the vial. The suspension was sonicated for 5 mins, to homogenously disperse the catalyst. Mesitylene (13.91 µL, 0.10 mmol), and benzyl alcohol (26.0 µL, 0.25 mmol) were injected into the reaction vial. The suspension was stirred for 30 mins in the dark to achieve equilibrium. 0.1 mL of the solution was then collected as initial reference. An $O_2$ balloon was used to ensure the atmospheric $O_2$ pressure was maintained at 0.1 MPa. The reaction vial was then placed in a 80 °C oil bath and irradiated with a 26 W Helical bulb for 24 hours.

The conversion was calculated using the following expression:

$$X(\%) = 100 \times \frac{C_0 - C_i}{C_0}$$

Where $X$ is the conversion, $C_0$ and $C_i$ are the molar concentrations of substrates before and after the photocatalytic reaction, respectively.

The turnover frequency (TOF) was calculated by the following expression:

$$TOF = \frac{\text{µmol of converted benzyl alcohol}}{[\text{reaction time in minutes}][\text{mass of Zr in gram}]}$$

The TOF is calculated based on per mass of Zr instead of per unit of the catalyst mass because the molar mass of the catalyst changes with different functionalized linker.

## 2.5 Results and discussion

The powder X-ray diffraction (PXRD) patterns (Fig. 1) show that the Zr-MOFs synthesized with mixed bridging linkers are crystalline and isoreticular to the parent Zr-MOF, UiO-66.[24]
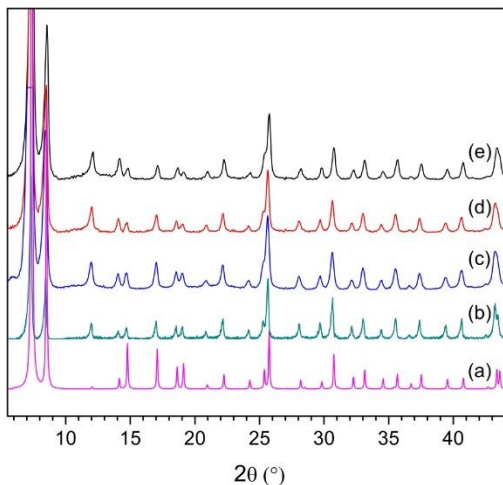


Fig. 1. PXRD patterns of (a) simulated UiO-66 and as-synthesized Zr-MOFs (b) UiO-66-NH$_2$, (c) UiO-66-NH$_2$-F, (d) UiO-66-NH$_2$-Cl, (e) UiO-66-NH$_2$-Br.

The porosity of the Zr-MOFs was evaluated by nitrogen adsorption and desorption isotherm (Fig. 2). The BET surface area of UiO-66-NH$_2$-H that consists of mixed linkers of BDC-H and BDC-NH$_2$ is 885 m$^2$/g. When the BDC-H linker is replaced by halide functionalized BDC, the BET surface area decreases. BET surface area for UiO-66-NH$_2$-F, UiO-66-NH$_2$-Cl and UiO-66-NH$_2$-Br are 871, 798, and 689 m$^2$/g respectively. The decrease in surface area indicates the incorporation of the halide-functionalized linkers in the Zr-MOF crystal. As the functional group gets bulkier, the total surface area decreases. However, the decrease in surface area of the Zr-MOFs made of mixed linkers cannot assure that each Zr-MOF crystal consisted of different linkers and not a physical mixture of two different functionalized Zr-MOFs.
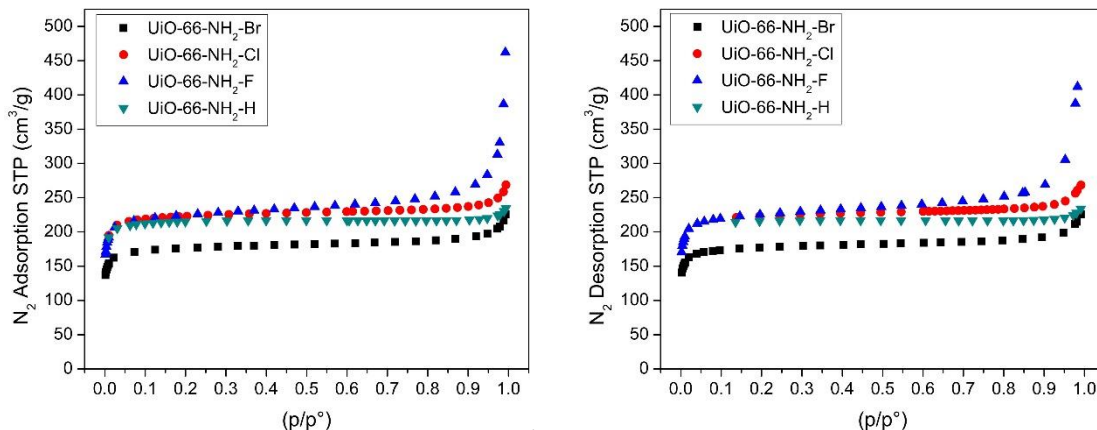
Fig. 2. Nitrogen adsorption (left) and desorption (right) isotherm of different Zr-MOFs at 77 K: (aqua) UiO-66-NH$_2$-H, (blue) UiO-66-NH$_2$-F, (red) UiO-66-NH$_2$-Cl, (black) UiO-66-NH$_2$-Br.

By utilizing two different linkers during the synthesis of Zr-MOF, it is possible to form two kinds of Zr-MOF crystals with pure linkers. This will result in a physical mixture of NH$_2$-functionalized Zr-MOFs and halide-functionalized Zr-MOFs. To investigate the distribution of the functionalized-linker, STEM and EDX analysis were done on UiO-66-NH$_2$-F. EDX analysis was performed on a selected area (Box 1) from the STEM (Fig. 3) which represents a single Zr-MOF crystal. The intensity at 0.39 keV and 0.68 keV in the EDX spectrum (Fig. 4) correspond to the *K*-edge of nitrogen and fluorine respectively. This indicates that both the fluorine- and amine-functionalized linkers are in fact present in a single Zr-MOF crystal.

Fig. 3. STEM image of mixed linker Zr-MOF, UiO-66-NH$_2$-F. Box 1 is a selected area representing a single Zr-MOF crystal.



Fig. 4. EDX spectrum of UiO-66-NH$_2$-F collected from area 1 as shown in the STEM image.
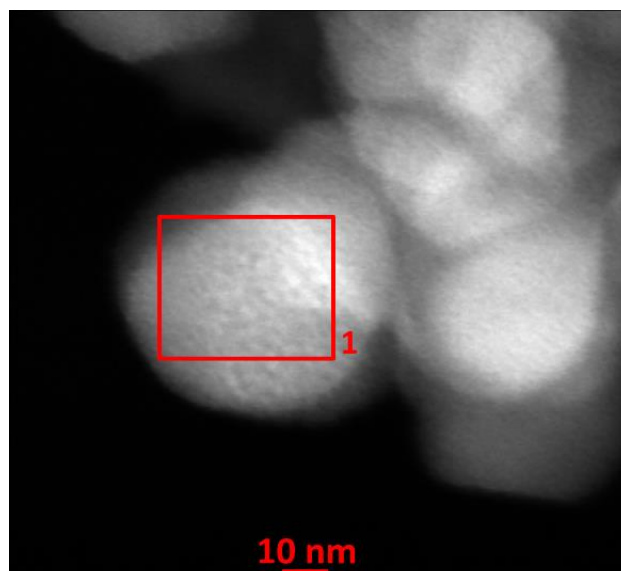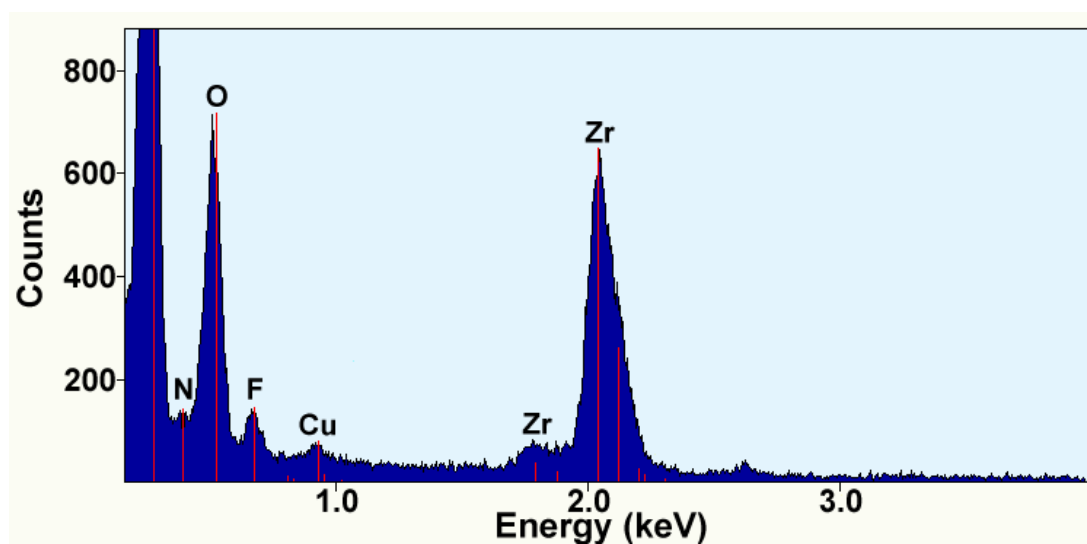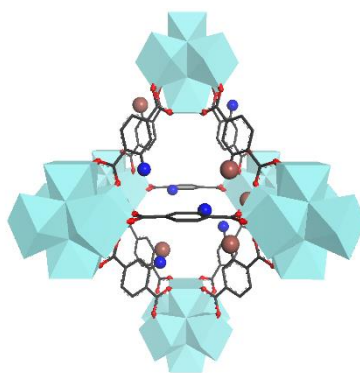
Scheme 2. Idealized molecular representation of mixed-linker Zr-MOF. Aqua polyhedrons represent the Zr-oxo cluster. Black, red, blue and brown represent carbon, oxygen, nitrogen and halides respectively. Hydrogen atoms omitted for clarity.

The mixed-linker UiO-66 MOFs were synthesized using a 1:1 molar ratio of 2-amino-1,4-benzenedicarboxylic acid and 2-X-1,4-benzenedicarboxylic acid (X = F, Cl, Br). Idealized molecular representation of mixed-linker Zr-MOF is shown in Scheme 2. To quantify the actual composition of the mixed linkers in these Zr-MOFs, we digested the Zr-MOFs in DMSO-$d_6$ and HF by sonication. The digested Zr-MOFs were analyzed by ^{1}H NMR (Fig. 5). Molar percentages of the different linkers are calculated from the integration of their appropriate proton peaks ($\delta =7.38$ for BDC-NH$_2$, $\delta =7.96$ for BDC-Br, $\delta =7.34$ for BDC-Cl and $\delta =7.70$ for BDC-F) are shown in Table 1. From the NMR analysis of these digested Zr-MOFs, we found that the composition of the mixed-functional linkers in these Zr-MOFs is close to the theoretical value. Among the three amino-halide mixed-linker Zr-MOFs, F-BDC linkers show the highest incorporation efficiency into the UiO-66 frameworks compared to the Cl- and Br-BDC linkers, which could be due to the relatively higher p$K_a$ values of the carboxylate groups on the F-BDC linkers.[29]
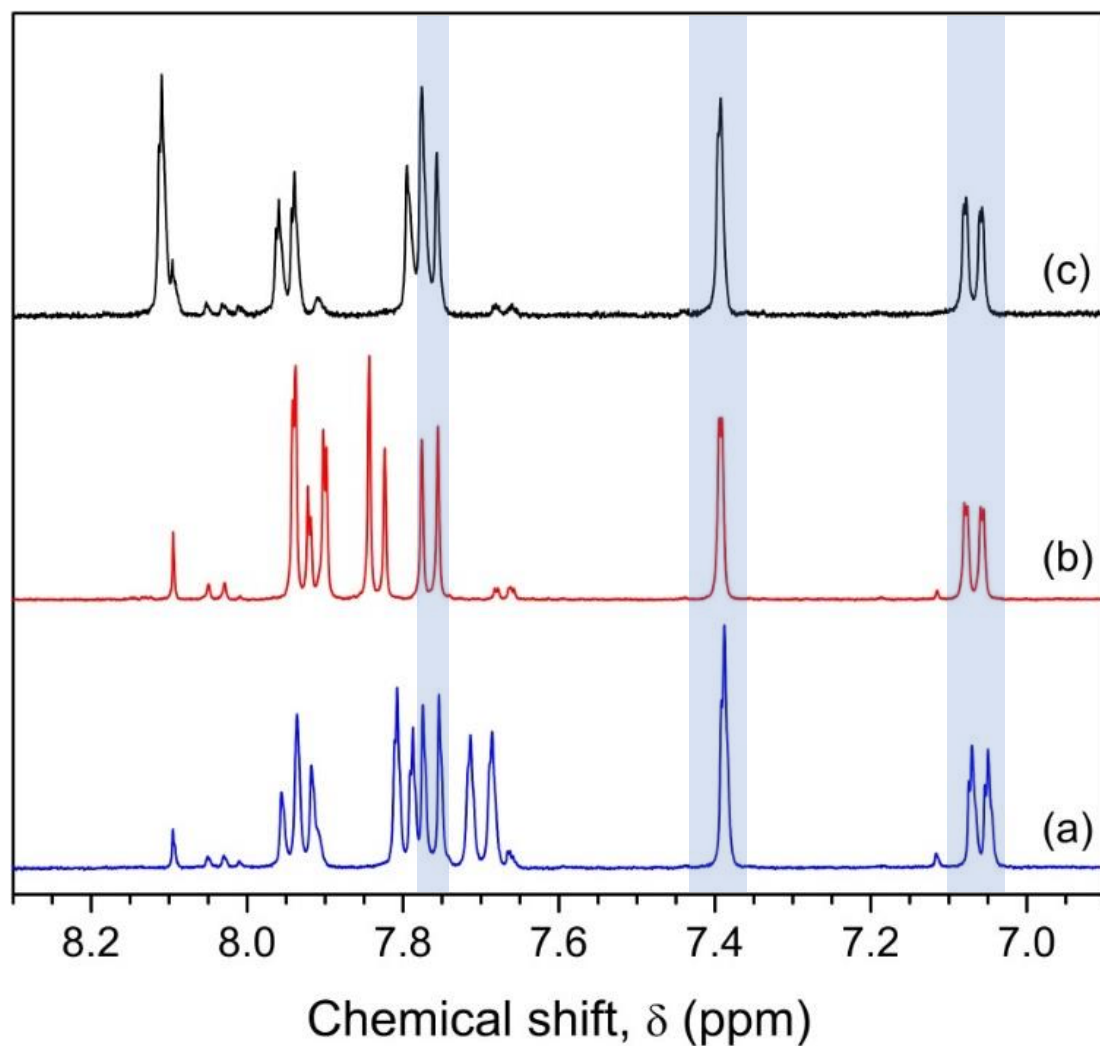
Fig. 5. $^1$H NMR spectrum of digested Zr-MOFs. (a) UiO-66-NH$_2$-F, (b) UiO-66-NH$_2$-Cl, (c) UiO-66-NH$_2$-Br. Highlighted peaks correspond to the aromatic protons on BDC-NH$_2$. Peaks at $\delta$ = 8.1 correspond to proton from DMF solvents.

**Table 1: BDC-X linker composition in Zr-MOFs measured by $^1$H NMR.**

| Entry | Catalyst | -NH$_2$ (mol%)[a] | -X (mol%)[a] | pK$_a$ X-BDC[b] |
|-------|----------|--------------------|---------------|------------------|
| 1 | UiO-66-NH$_2$-F | 43.1 | 56.9 | 2.86 |
| 2 | UiO-66-NH$_2$-Cl | 46.9 | 53.1 | 2.45 |
| 3 | UiO-66-NH$_2$-Br | 47.2 | 52.8 | 2.44 |

[a] Calculated by peak area of NH$_2$-BDC to X-BDC linkers (X = F, Cl, Br)

[b] pK$_a$ values are obtained from SciFinder database.

The presence of multi-functionalities in the Zr-MOFs was also confirmed by DRIFTS (Fig. 6). The presence of amino group in all samples was clearly evident by the vibrations at ~3380 and ~3510 cm$^{-1}$, corresponding to the aromatic N-H stretching modes.[30] The presence of the halogen functional groups in UiO-66-NH$_2$-X (X= F, Cl, Br) is indirectly supported by the vibration at the 1000 – 1150 cm$^{-1}$ region. This vibration corresponds to the enhanced in-plane C-H bending mode of the aromatic ring with substituted halogen groups.[30]
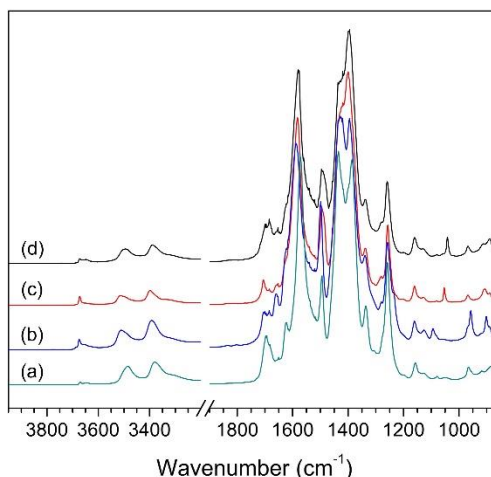
Fig.6. DRIFTS spectrum of as-synthesized Zr-MOFs. (a) UiO-66-NH$_2$, (b) UiO-66-NH$_2$-F, (c) UiO-66-NH$_2$-Cl, (d) UiO-66-NH$_2$-Br.

Each Zr-MOFs show a strong absorbance peak circa 420 nm that is within the visible light absorbance spectrum (Fig. 6). This absorbance is due to the presence of amino group on the benzene ring that acts as an auxochromic and bathochromic group.[31] The lone pair of electrons on the amino group donates electron density to the lowest unoccupied molecular orbital (LUMO) of the benzene ring (an anti-bonding orbital).[32] This significantly shifts the highest occupied molecular orbital (HOMO) to a higher energy, which causes the decrease in band gap energy, $E_g$ of the linker. Since the optical response of MOFs is ligand-to-metal charge transfer (LCMT) in character, the band gap shift of the linker influence the optical response of the MOF.[33,34] The band gap of all the catalysts was calculated based on the formula $E_g = 1240/\lambda$. All Zr-MOFs show a similar band gap of 2.75 eV with similar peak intensity (Figure 7). As predicted by Hendon and coworkers,[34] introduction of strong electron-donating functional group such as amine will significantly reduce the band gap of the MOFs. Considering that aromatic halide can either be weakly electron-withdrawing or

weak electron-donating, the overall effects in the mixed-linker Zr-MOFs is imperceptible and couldn't be resolved by our instrument.
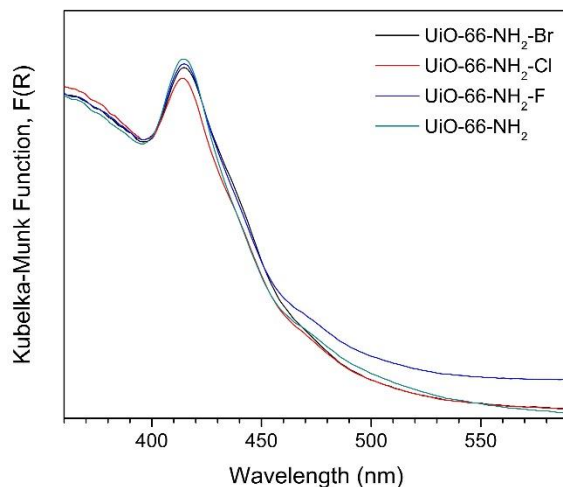


Fig. 7. UV-visible diffuse reflectance spectra of Zr-MOFs. (aqua) UiO-66-NH$_2$, (blue) UiO-66-NH$_2$-F, (red) UiO-66-NH$_2$-Cl, (black) UiO-66-NH$_2$-Br.

The visible light photocatalytic activity of these Zr-MOFs was evaluated in benzyl alcohol oxidation utilizing a 26 W helical light bulb as the visible light source. The spectrum of the light source was measured (Fig. 8). The irradiation peaks from 400 nm to 700 nm are within the visible-light region. All the catalysts showed high selectivity towards benzaldehyde (>99%), no over-oxidized product was observed (Entries 4-8). In the absence of either the catalysts (entry 1) or the visible light (entry 9),less than 1% conversion was observed for the benzyl alcohol oxidation. Control experiments performed with UiO-66 (Table 2, Entry 2) and UiO-66-F (Table 2, Entry 3) in the presence of visible light showed no significant activity, indicating the importance of NH$_2$-BDC linkers as visible light antennae.

**Table 2: Benzyl alcohol oxidation catalyzed by Zr-MOFs.[a]**



| Entry | Catalyst | MOF[b] (mmol) | Conv.[c] (%) | TOF[e] ($\mu$mol min$^{-1}$ g$^{-1}$) |
|:---:|:---|:---:|:---:|:---:|
| 1 | Blank | - | <1 | - |
| 2 | UiO-66 | 0.10 | <1 | - |
| 3 | UiO-66-F | 0.10 | <1 | - |
| 4 | UiO-66-NH$_2$ | 0.10 | 18.4 | 140 |
| 5 | UiO-66-NH$_2$-H | 0.10 | 11.7 | 89 |
| 6 | UiO-66-NH$_2$-F | 0.10 | 53.9 | 410 |
| 7 | UiO-66-NH$_2$-Cl | 0.10 | 38.2 | 290 |
| 8 | UiO-66-NH$_2$-Br | 0.10 | 43.4 | 330 |
| 9[d] | UiO-66-NH$_2$-Br | 0.10 | <1 | - |

[a] Reaction conditions: 0.25 mmol Benzyl alcohol, 0.1 mmol mesitylene in 3 mL toluene, 0.1 MPa O$_2$, heated at 80 °C for 24 h, irradiated with 26 W helical light bulb.

[b] Based on Zr content.

[c] Conversion as determined by GC using mesitylene as the internal standard. The selectivity to benzaldehyde is > 99%.

[d] Reaction was performed in the absence of light.

[e] Average turnover frequencies.

The conversion of benzyl alcohol using UiO-66-NH$_2$ (Table 2, Entry 4) as the catalyst is 18.4% in 24 hours. When the concentration of NH$_2$-BDC linkers was reduced by half as in UiO-66-NH$_2$-H (which only contains 45% NH$_2$-BDC, the remaining 55% of the linker is H-BDC), the conversion of benzyl alcohol decreased byalmost half to 11.7% (Table 2, Entry 5). Considering the amount of Zr is the same in both cases (Table 2, Entry 4-5), the decreased conversion in UiO-66-NH$_2$-H indicates NH$_2$-BDC plays an important role in the visible light photo-excitation of electrons. Electron paramagnetic resonance (EPR) studies done by Long et. al[16] indicated that upon visible light irradiation, the electrons from the HOMO (O, C and N 2p orbitals) of the amine-functionalized Zr-MOFs were excited and transferred to the O$_2$ molecules absorbed on the Zr$^{3+}$ sites to form •O$_2^-$ radicals. The •O$_2^-$ radicals could further react with the benzylic cations that form upon reaction of benzyl alcohols with the photo-generated holes on the amino groups on the BDC linkers.
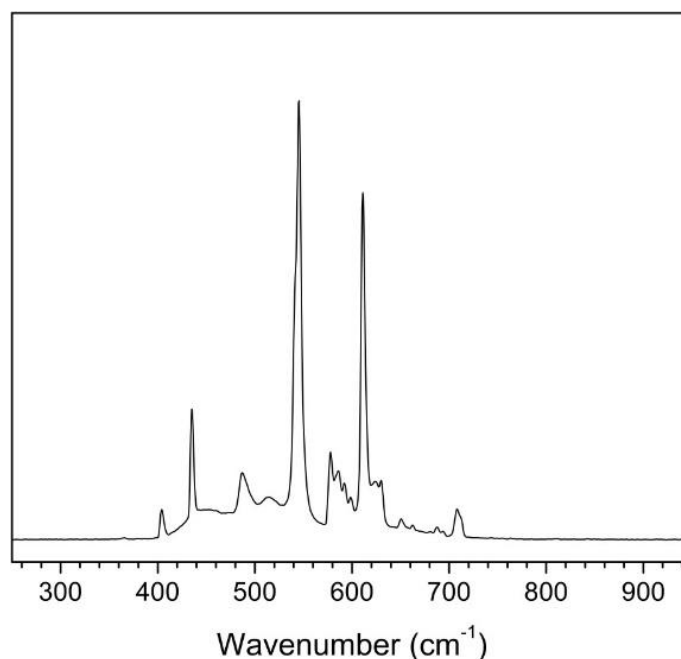


Fig. 8. Spectrum of the 26W helical light bulb used in the photocatalytic reaction.

To improve the catalytic activity of Zr-MOFs in the oxidation of benzyl alcohol, we introduced secondary linker during the synthesis of Zr-MOFs as depicted in Scheme 1. Noteworthy, in all these mixed-linker UiO-66 MOFs, is that the locations of the different linkers are randomly allocated because the Zr-MOFs are solid-solutions.[35] However, all the secondary linkers introduced into these Zr-MOFs do not absorb visible light. These Zr-MOF catalysts with mixed linkers show marked increase in the conversion of benzyl alcohol as noted in Table 2 (Entry 6-8).

Upon the replacement of H-BDC linkers with halogenated linkers (X-BDC, X=F, Cl, Br), the benzyl alcohol oxidation activity of the Zr-MOFs showed a four- to five-fold enhancement in comparison to UiO-66-NH$_2$-H. This could be due to the stabilization of the •O$_2$$^-$ radical on the Zr$^{3+}$ by the halogenated linkers, which decreases the recombination rate of the photogenerated electrons and holes. This enhancement in catalytic activity could also be related to the preferential interaction of the halogen groups with benzyl alcohol molecules that drives the equilibrium of the reaction to benzaldehyde. Molecular modeling studies carried out by Vermoortele et al. showed that different linkers with different electronic properties incorporated into Zr-MOFs could stabilize the reactants and intermediates, which led to the high conversion in the cyclization of citronellal.[25]

### 2.6 Conclusion

In conclusion, we successfully developed mixed-linker Zr-MOF photocatalysts with enhanced activity in benzyl alcohol oxidation. The crystallinity of the as-synthesized Zr-MOFs which is isoreticular to UiO-66 was confirmed by powder X-ray diffraction. All the Zr-MOFs have high surface area and porosity. The surface area decreases as the size of the

functional group increases. EDX analysis indicates that a single UiO-66-NH$_2$-F crystal contained both N and F atoms which indicates the presence of both NH$_2$-BDC and F-BDC linkers in a single Zr-MOF crystal. This excludes the possibility that the as-synthesized Zr-MOFs are physical mixture. The NMR studies of the digested Zr-MOFs show that the composition of the linkers is close to 1:1 molar ratio. The presence of different functional groups in the Zr-MOFs was further confirmed by diffuse reflectance infrared spectroscopy analysis through the specific vibration of each functional group. Partial substitution of the primary NH$_2$-BDC by electron-withdrawing halogenated BDC linkers enhanced the photocatalytic activity of the Zr-MOFs. We demonstrated that using mixed linkers with different functionalities to facilitate the design of efficient MOF catalysts is a promising direction. Further studies to understand the enhanced conversion with isoreticular UiO-66 MOFs of mixed linkers and to further improve their performance are underway.

## 2.6 References

(1)     Fujishima, A.; Honda, K. *Nature* **1972**, *238*, 37.

(2)     Linsebigler, A. L.; Lu, G.; Yates, J. T. *Chemical Reviews* **1995**, *95*, 735.

(3)     Duncan, W. R.; Prezhdo, O. V. *Annual Review of Physical Chemistry* **2007**, *58*, 143.

(4)     Kamat, P. V. *The Journal of Physical Chemistry C* **2008**, *112*, 18737.

(5)     Peng, H.-Q.; Chen, Y.-Z.; Zhao, Y.; Yang, Q.-Z.; Wu, L.-Z.; Tung, C.-H.; Zhang, L.-P.; Tong, Q.-X. *Angewandte Chemie International Edition* **2012**, *51*, 2088.

(6)     Suh, M. P.; Park, H. J.; Prasad, T. K.; Lim, D.-W. *Chemical Reviews* **2011**, *112*, 782.

(7)     Kuo, C.-H.; Tang, Y.; Chou, L.-Y.; Sneed, B. T.; Brodsky, C. N.; Zhao, Z.; Tsung, C.-K. *Journal of the American Chemical Society* **2012**, *134*, 14345.

(8)     Gascon, J.; Corma, A.; Kapteijn, F.; Llabrés i Xamena, F. X. *ACS Catalysis* **2013**, 361.

(9)     Li, J.-R.; Kuppler, R. J.; Zhou, H.-C. *Chemical Society Reviews* **2009**, *38*, 1477.

(10)    Zhuang, J.; Kuo, C.-H.; Chou, L.-Y.; Liu, D.-Y.; Weerapana, E.; Tsung, C.-K. *ACS Nano* **2014**, *8*, 2812.

(11)    Kreno, L. E.; Leong, K.; Farha, O. K.; Allendorf, M.; Van Duyne, R. P.; Hupp, J. T. *Chem. Rev.* **2011**, *112*, 1105.

(12)    Eddaoudi, M.; Kim, J.; Rosi, N.; Vodak, D.; Wachter, J.; O'Keeffe, M.; Yaghi, O. M. *Science* **2002**, *295*, 469.

(13)    Alvaro, M.; Carbonell, E.; Ferrer, B.; Llabrés i Xamena, F. X.; Garcia, H. *Chemistry – A European Journal* **2007**, *13*, 5106.

(14)    Gascon, J.; Hernández-Alonso, M. D.; Almeida, A. R.; van Klink, G. P. M.; Kapteijn, F.; Mul, G. *ChemSusChem* **2008**, *1*, 981.

(15)    Fu, Y.; Sun, D.; Chen, Y.; Huang, R.; Ding, Z.; Fu, X.; Li, Z. *Angewandte Chemie International Edition* **2012**, *51*, 3364.

(16)    Long, J.; Wang, S.; Ding, Z.; Wang, S.; Zhou, Y.; Huang, L.; Wang, X. *Chemical Communications* **2012**, *48*, 11656.

(17)    Nasalevich, M. A.; Goesten, M. G.; Savenije, T. J.; Kapteijn, F.; Gascon, J. *Chemical Communications* **2013**, *49*, 10575.

(18)    Nasalevich, M.; van der Veen, M. A.; Kapteijn, F.; Gascon, J. *CrystEngComm* **2014**.

(19)    Wang, C.; Xie, Z.; deKrafft, K. E.; Lin, W. *Journal of the American Chemical Society* **2011**, *133*, 13445.

(20) Burrows, A. D.; Frost, C. G.; Mahon, M. F.; Richardson, C. *Angewandte Chemie International Edition* **2008**, *47*, 8482.

(21) Deng, H.; Doonan, C. J.; Furukawa, H.; Ferreira, R. B.; Towne, J.; Knobler, C. B.; Wang, B.; Yaghi, O. M. *Science* **2010**, *327*, 846.

(22) Marx, S.; Kleist, W.; Huang, J.; Maciejewski, M.; Baiker, A. *Dalton Transactions* **2010**, *39*, 3795.

(23) Taylor-Pashow, K. M. L.; Rocca, J. D.; Xie, Z.; Tran, S.; Lin, W. *Journal of the American Chemical Society* **2009**, *131*, 14261.

(24) Cavka, J. H.; Jakobsen, S.; Olsbye, U.; Guillou, N.; Lamberti, C.; Bordiga, S.; Lillerud, K. P. *Journal of the American Chemical Society* **2008**, *130*, 13850.

(25) Vermoortele, F.; Vandichel, M.; Van de Voorde, B.; Ameloot, R.; Waroquier, M.; Van Speybroeck, V.; De Vos, D. E. *Angewandte Chemie International Edition* **2012**, *51*, 4887.

(26) Meek, S. T.; Perry, J. J.; Teich-McGoldrick, S. L.; Greathouse, J. A.; Allendorf, M. D. *Crystal Growth & Design* **2011**, *11*, 4309.

(27) Guo, Z.; Xiao, C.; Maligal-Ganesh, R. V.; Zhou, L.; Goh, T. W.; Li, X.; Tesfagaber, D.; Thiel, A.; Huang, W. *ACS Catalysis* **2014**, 1340.

(28) Walton, K. S.; Snurr, R. Q. *Journal of the American Chemical Society* **2007**, *129*, 8552.

(29) DeCoste, J. B.; Peterson, G. W.; Jasuja, H.; Glover, T. G.; Huang, Y. G.; Walton, K. S. *Journal of Materials Chemistry A* **2013**, *1*, 5642.

(30) Coates, J. In *Encyclopedia of Analytical Chemistry*; John Wiley & Sons, Ltd: 2006.

(31) Gomes Silva, C.; Luz, I.; Llabrés i Xamena, F. X.; Corma, A.; García, H. *Chemistry – A European Journal* **2010**, *16*, 11133.

(32) Wojciechowski, P. M.; Zierkiewicz, W.; Michalska, D.; Hobza, P. *The Journal of Chemical Physics* **2003**, *118*, 10900.

(33)  Civalleri, B.; Napoli, F.; Noel, Y.; Roetti, C.; Dovesi, R. *CrystEngComm* **2006**, *8*, 364.

(34)  Hendon, C. H.; Tiana, D.; Fontecave, M.; Sanchez, C.; D'arras, L.; Sassoye, C.; Rozes, L.; Mellot-Draznieks, C.; Walsh, A. *Journal of the American Chemical Society* **2013**, *135*, 10942.

(35)  Kong, X.; Deng, H.; Yan, F.; Kim, J.; Swisher, J. A.; Smit, B.; Yaghi, O. M.; Reimer, J. A. *Science* **2013**, *341*, 882.

# CHAPTER 3.   SPECTROSCOPY IDENTIFICATION OF BIMETALLIC SURFACE OF PTSN NANOCLUSTER ENCAPSULATED IN METAL-ORGANIC FRAMEWORK FOR SELECTIVE FURFURAL HYDROGENATION

*Manuscript submitted*

Tian Wei Goh, Prof. Chia-Kuang Tsung, Prof. Wenyu Huang

## 3.1 Abstract

The development of bimetallic nanoparticles has gained great interest over their monometallic counterparts due to their distinct and unique properties in a wide range of applications such as catalysis, energy storage, and bio/plasmonic imaging. Identification and characterization of these bimetallic entities remain a challenge and heavily rely on advanced characterization techniques such as aberration-corrected microscopy, and synchrotron X-ray absorption studies. In this article, we reported a strategy to synthesize sub 2-nm bimetallic Pt-Sn nanoclusters confined in the pores of a Zr-based metal-organic framework. We demonstrate a quick and convenient surface sensitive characterization technique utilizing diffuse reflectance infrared Fourier transform spectroscopy of adsorbed CO to probe the bimetallic surface of the encapsulated ultrafine Pt-Sn nanocluster. Complementary techniques such as aberration-corrected high-angle annular dark field scanning transmission electron microscopy with energy dispersive X-ray spectroscopy and X-ray photoelectron spectroscopy were used to characterize the Pt-Sn nanoclusters. The Pt-Sn nanoclusters show enhanced chemoselectivity in an industrially relevant reaction, furfural hydrogenation.

## 3.2 Introduction

Shifting reliance from fossil fuels and chemicals towards green ones is critical towards keeping global warming below 1.5 °C and countering unfavorable climate changes. The increasing demand in the agrochemical, flavor/fragrance, chemicals, and pharmaceutical industries has prompt the derivatization of unsaturated alcohols through selective hydrogenation of renewable biofuel derived α,β-unsaturated aldehydes [1-2] One of the most common industrial commodity chemicals, furfuryl alcohol, has a global market of US$ 836.2 million and a yearly growth rate of 4.5% that are expected to reach US$ 1.4 billion by 2028. Global production of furfuryl alcohol consumed about 60-62% of the world annual furfural feedstock that is more than 280 kilotons.[3] There is a strong need for the development of effective catalysts for this transformation. However, the chemoselective hydrogenation of furfural to furfuryl alcohol is challenging because selective hydrogenation of the C=O bond is thermodynamically less favorable than C=C bond by about 35 kJ/mol.[4-5]

For years, industrial production of furfuryl alcohol utilizes nickel and copper chromite-based catalyst to selectively hydrogenate furfural.[6] However, possible chromium-caused environment pollution and the adverse effect on public health[7] have led to the exploration and development of alternative monometallic catalyst based on Pt, Pd, Rh, and Ni supported on metal oxides.[8-9] The chemoselectivity of these supported catalysts is strongly influenced by the support-metal interaction at the interfaces, and the synergistic effect between the adjacent atoms.[10-11] Intuitively, to increase the number of catalytic active sites, it is essential to maximize the metal-support boundary, by minimizing the size of the metal nanoparticles. Recently, Tang et al. showed that sandwiching a pre-synthesized 2.8 nm Pt nanoparticles between highly porous metal-organic frameworks (MOFs) can serve as effective selectivity regulators for the hydrogenation of α,β-unsaturated aldehydes in the

liquid phase.[12] Tang and Hu groups have also shown that micro- and mesoporous polymer coating on the Pt nanoparticles supported on the exterior of MIL-101 can improve the selective hydrogenation of cinnamaldehyde to cinnamyl alcohol.[13]

We proposed that direct modifications of the Pt nanocluster surface by a secondary metal could provide selectivity enhancement in furfural hydrogenation through a facile approach, thus circumventing those tedious multistep synthetic methods. Previously, we have shown that Pt nanoclusters can be stabilized within the pore of the amino-functionalized MOFs through extensive microscopy and spectroscopy studies.[14-16] However, characterizing the bimetallic surface of nanoclusters remains a challenging topic in surface science and catalysis. Surface techniques such as X-ray photoelectron spectroscopy typically conducted under high-vacuum, may not be a realistic representation of the metastable surface during catalytic reactions. While high angle annular dark field scanning transmission electron microscopy (HAADF-STEM) provide statistically limited information, due to the analysis of a limited percentage of the overall sample.[17]

In this work, we show that the Pt-Sn nanoclusters with a bimetallic surface can be formed within the pore of the MOFs through successive impregnation of Sn into cavity-confined Pt nanoclusters in UiO-66-NH$_2$. The formation of Pt-Sn bimetallic nanoclusters was extensively investigated using scanning transmission electron microscopy (STEM), energy dispersive X-ray spectroscopy (EDS), and X-ray photoelectron spectroscopy (XPS). We also confirmed that the Pt-Sn nanoclusters have a bimetallic surface with isolated Pt sites using diffuse reflectance infrared Fourier-transform spectroscopy (DRIFTS) with carbon monoxide as the surface probe molecules. The introduction of Sn to the Pt nanoclusters confined in the

MOF cavities show significant improvement in the selective hydrogenation of furfural towards furfural alcohol.

## 3.3 Experimental Section

Synthesis of UiO-66-NH$_2$

$ZrCl_4$ (170 mg, 0.73 mmol), and 2-aminoterephthalic acid (132 mg, 0.73 mmol) was dissolved in a solution containing 38 mL of N,N-dimethylformamide (DMF), and 2.1 mL of glacial acetic acid. The solution was then capped and heated at 120 °C for 24 hours. Yellow precipitate was obtained and isolated by centrifugation at 8100 rcf, washed with copious amount of DMF and acetone. The yellow solid was dried at 80 °C in air.

Encapsulation of Pt nanocluster in UiO-66-NH$_2$ (Pt@UiO-66-NH$_2$)

UiO-66-NH$_2$ (200 mg) was dispersed in 12 mL of H$_2$O by sonication to form a yellow suspension. An aqueous solution (2 mL) of the appropriate concentration of K$_2$PtCl$_4$ was added dropwise to the yellow suspension while stirring vigorously at room temperature. The suspension was magnetically stirred for 24 hours. The Pt$^{2+}$ impregnated solid was isolated by centrifugation at 2100 rcf for 5 minutes. The solid was washed with copious amount of water and acetone before drying at 80 °C in air. The solid was further treated under a dynamic flow of 10%H$_2$/Ar (50 mL/min) for an hour at 200 °C.

Incipient wetness impregnation of Sn into Pt@UiO-66-NH$_2$ (PtSn@UiO-66-NH$_2$)

PtSn@UiO-66-NH$_2$ was synthesized using an incipient wetness impregnation (IWI) method. For 100 mg of Pt@UiO-66-NH$_2$, 80 µL of an ethanolic solution containing an appropriate amount of SnCl$_2$ was added to the solid. The solid was grind for five minutes to

form a homogeneous powder. The powder was further reduced at 200° C for 2 hours to form

Pt-Sn@UiO-66-NH$_2$.

## 3.4 Material Characterizations

Powder X-ray diffraction (PXRD) pattern was recorded at room temperature using a

Bruker D8 Advance diffractometer with Ni-filtered Cu Kα radiation (1.5418 Å) at 40 kV and

40 mA. Inductively coupled plasma mass spectrometry (ICP-MS) measurement was carried

out using a Thermo Fisher Scientific X Series 2 spectrometer. Transmission electron

microscopy (TEM) images were obtained using a Tecnai G2-F20 operated at 200 kV. High-

resolution high-angle annular dark field scanning transmission electron microscopy (HAADF

STEM) imaging was performed on a Titan Themis 300 aberration-corrected electron

microscope with a Super-X EDX detector. X-ray photoelectron spectroscopy (XPS)

measurements were performed on Kratos Analytical Amicus X-ray photoelectron

spectrometer using monochromatized Al Kα (1486.7 eV) as the excitation source. N$_2$

physisorption analysis was performed on a Micromeritics 3Flex surface characterization

analyzer at 77 K.

## 3.5 Diffuse Reflectance infrared spectroscopy (DRIFTS) of adsorbed CO

The diffuse reflectance infrared Fourier transform spectroscopy (DRIFTS) spectra

were collected using an Agilent Cary 670 FTIR equipped with a linearized Mercury-

Cadmium-Telluride (MCT) detector, a Harrick diffuse reflectance accessory, and a Praying

Mantis high-temperature reaction chamber. About 20 mg of the powder sample is packed

into the IR sample holder equipped with KBr windows. All spectra were obtained at a

resolution of 2 cm$^{-1}$ from 700 – 4000 cm$^{-1}$ under atmospheric pressure. The sample was first

heated to 200 °C in a dynamic He flow (40 mL/min) to remove any adsorbed CO molecules from the sample surface. After cooling to 30 °C, a spectrum of the sample was recorded as a background under He atmosphere. Carbon monoxide (100 Torr) was introduced into the He flow for 30 minutes to reach an equilibrium state. The gas phase carbon monoxide was purged from the cell under a dynamic He flow for 30 minutes. A spectrum of the adsorbed carbon monoxide on the surfaces was obtained. The IR spectra were collected continuously at variable temperatures under a constant He flow.

### 3.6 Continuous gas phase hydrogenation of furfural

The catalytic performance of the Pt-Sn nanocluster encapsulated in UiO-66-NH$_2$ for furfural hydrogenation was evaluated in a home-built plug flow reactor. Typically, about 5 mg of solid catalysts (0.21 mg of Pt, 0.001 µmol Pt) was diluted in 200 mg of low surface area quartz sand and loaded into a quartz reactor bed. Prior to the reaction, the catalyst was pre-reduced in-situ under 10% H$_2$/He (He/H$_2$ = 45/5 mL min-1) at 200 °C for 2 hours. After pre-treatment, the reactor was cooled down to 160 °C while purging the reactor with He. The reaction gas mixture composed of 0.023 mL/min of furfural vapor (8.6 mL/min He through a furfural bubbler) and 11.4 mL/min H$_2$ at atmospheric pressure was passed through the catalyst bed. The vapor from the reactor outlet was analyzed using an on-line HP 5890 gas chromatography equipped with a capillary column (DB-5, 30 m $\times$ 0.32 mm $\times$ 0.25 µm) and a flame ionization detector.

### 3.7 Results and discussion

MOFs have been extensively employed as solid supports for the encapsulation of various nano-entities.[18-19] Due to the well-defined pore size and geometry of MOFs,

monodisperse nanoparticles can be formed within the periodically confined space. Xu et al. demonstrated an elegant approach of using double solvents to drive the formation of Pt nanocluster in the cavity of MIL-101, while Li et al. has demonstrated a de novo approach in the synthesis of Pd and Pd/Ag nanoparticles in the pores of UiO-67 utilizing bipyridine linkers.[20-22] Independently, our group has successfully synthesized monodispersed sub 2-nm monometallic Pt and Pd nanoclusters confined within a Zr-based MOFs through post-synthetic wetness impregnation using potassium tetrachloroplatinate and palladium acetate as the metal precursors, respectively.[16, 23] The precise immobilization of metals into the MOF cages was driven by the preferential interaction between the nitrogen donors on the organic linkers with the metal precursor ions as studied extensively by our group using X-ray absorption spectroscopy (XAS) and solid-state nuclear magnetic resonance (ssNMR).[14-15, 24]
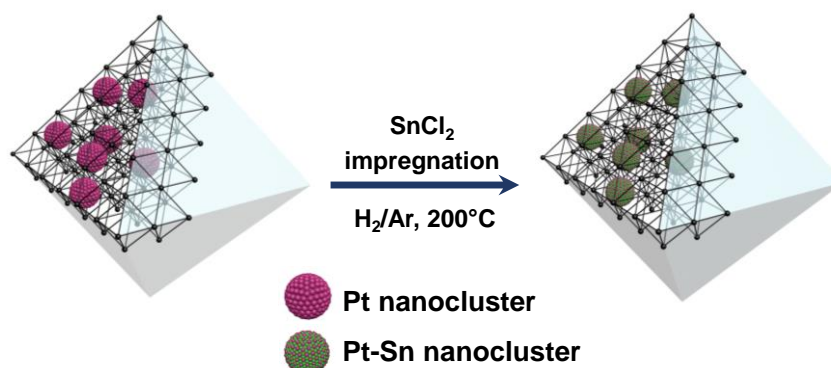


**Figure 1.** Schematic illustration of the preparation of Pt-Sn nanoclusters from Pt nanoclusters in UiO-66-NH$_2$ through the impregnation of SnCl$_2$ followed by a gas-phase reduction in H$_2$/Ar at 200 °C.

The synthesis of Pt-Sn nanocluster encapsulated in UiO-66-NH$_2$ is illustrated in Figure 1. UiO-66-NH$_2$, a zirconium-based MOF, was chosen as the support due to its' superior thermal and chemical stability. The stability of UiO-66-NH$_2$ roots from its' high

charge density and bond polarization between the Zr(IV) metal nodes and the carboxylates group of the organic linkers.[25-28] The ultrafine Pt nanoclusters encapsulated in UiO-66-NH$_2$ (Pt@UiO-66-NH$_2$) was first prepared according to our previously reported method.[16] The confinement of Pt in the cavity of the UiO-66-NH$_2$ was thoroughly investigated in our previous studies, using variable-angle TEM analysis, where no observable Pt nanocluster at the periphery of UiO-66-NH$_2$ during the tilting of the MOF particles.[16] We also performed hydrogenation of cycloalkene using probe molecules of various sizes to confirmed the active Pt nanocluster is indeed confined in the cage.[16] After the formation of Pt nanoclusters through a 200 °C reduction in 50 mL min$^{-1}$ 10% H$_2$/Ar dynamic gas flow, an ethanolic solution of Sn$^{2+}$ was impregnated into the Pt@UiO-66-NH$_2$ based on the Pt content (3.9 ± 0.2 wt% as determined by ICP-MS). After another 200 °C gas-phase reduction for 2 hours under the same condition, we synthesized Pt-Sn@UiO-66-NH$_2$.

After impregnation of Sn and subsequent reduction treatment, the size of the nanoclusters remains small (1.6 ± 0.3 nm) (Figure 2A-B) relative to the Pt seeds (1.4 ± 0.2 nm) (Figure S1). This could be due to the pore-confinement effect from the MOF that limits the growth of the nanoclusters. The homogeneous dispersion of Pt and Sn elements in the UiO-66-NH$_2$ framework was confirmed by high-angle annular dark-field scanning transmission electron microscopy (HAADF-STEM) images and energy dispersive X-ray spectroscopy (EDS) elemental mapping (Figure 2). In the HAADF-STEM image (Figure 2C), ultrafine bright dots appear to disperse homogenously within the framework. HAADF-STEM allows the collection of Rutherford scattered electrons exclusively, and thus heavy atoms such as Pt and Sn with higher intensity of scattered electrons appear to be brighter.[29] EDS elemental mapping was performed to identify the chemical composition of those bright

dots in Figure 2C. Figure 2D-F shows that the Pt and Sn are in fact dispersed homogeneously within the nanocrystal after 200 °C reduction in 10%$H_2$/Ar. EDS line scan (Figure S2) confirmed that both the Pt and Sn is within proximity forming Pt-Sn nanoclusters.
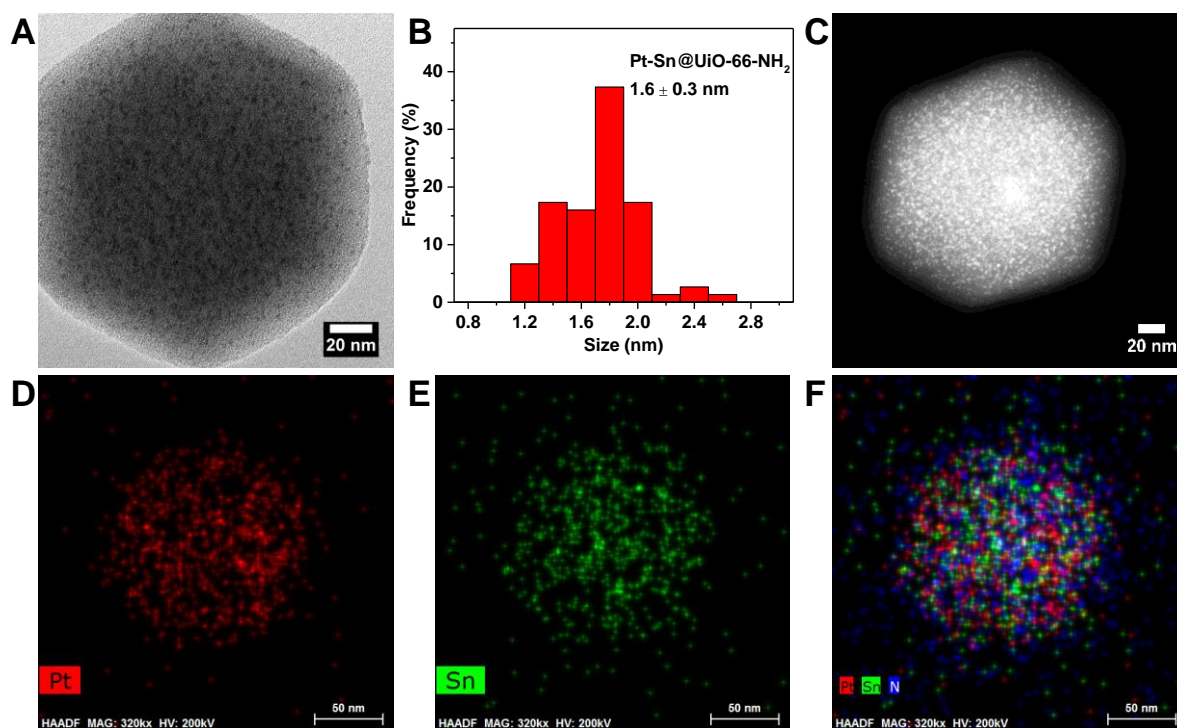


**Figure 2.** Electron microscopy analysis of Pt-Sn nanoclusters confined in the cavities of UiO-66-$NH_2$. (A) A bright-field TEM image of Pt-Sn@UiO-66-$NH_2$. (B) Particle size distribution of Pt-Sn nanoclusters encapsulated in UiO-66-$NH_2$. (C) A representative HAADF-STEM image of a Pt-Sn@UiO-66-$NH_2$ particle. (D-F) Elemental mappings that show the distributions of Pt, Sn, and Pt+Sn+N of the Pt-Sn@UiO-66-$NH_2$ particle displayed in (C).

Although STEM-EDX mapping shows that the Pt and Sn are in close spatial proximity, we cannot conclude that Pt and Sn form bimetallic nanoclusters. Further $N_2$

physisorption analysis at 77 K shows that there is no significant decrease in surface area of the highly porous Zr metal-organic framework (Figure S3, Table S1). This eliminates the possibility that the pores were clogged by $SnO_2$ during the synthesis of Pt-Sn nanoclusters from Pt@UiO-66-NH$_2$.

In order to examine the atomic interaction between Sn and Pt, we performed X-ray photoelectron spectroscopy (XPS) analysis on the Pt@UiO-66-NH$_2$ and Pt-Sn@UiO-66-NH$_2$. All binding energies were calibrated using the C 1s line at 284.6 eV, which provide binding energy value with an accuracy of ±0.2 eV.[30] The Pt 4f XPS spectrum in Figure 3A shows that Pt nanoclusters confined in UiO-66-NH$_2$ exhibit two peaks, corresponding to metallic Pt$^0$ at 71.3 eV ($4f_{7/2}$) and 74.9 eV ($4f_{5/2}$).[16] Upon introduction of Sn into the Pt nanoclusters, the peaks correspond to Pt$^0$ binding energy shifted by less than 0.2 eV to 71.1 eV. This slight shift in the binding energy could indicate the electronic effect of Sn on Pt in forming Pt-Sn nanoclusters. The Sn 3d XPS spectrum (Figure S4) indicates the presence of both metallic and oxidized Sn with the Sn $3d_{5/2}$ peak at 484.4 eV and 486.3 eV respectively. Prior to ex-situ XPS analysis, the samples were freshly reduced at 200 °C, however, due to the oxophilic nature of Sn and the ultrasmall particle size, the Sn could be readily oxidized upon exposure to air. The Sn$^{2+}$ is readily reduced at 200°C in the presence of Pt, possibly facilitated by H atom spillover upon dissociation on Pt.[31-32] Powder X-ray diffraction (PXRD) patterns (Figure 3C) shows that upon subsequent reduction treatment to form PtSn bimetallic nanocluster in UiO-66-NH$_2$, the bulk crystallinity of the MOF remains unperturbed. Due to the small size of the encapsulated metal nanoclusters or the lack of crystalline bulk phase, the diffraction patterns for Pt and Pt-Sn phases were not observed.
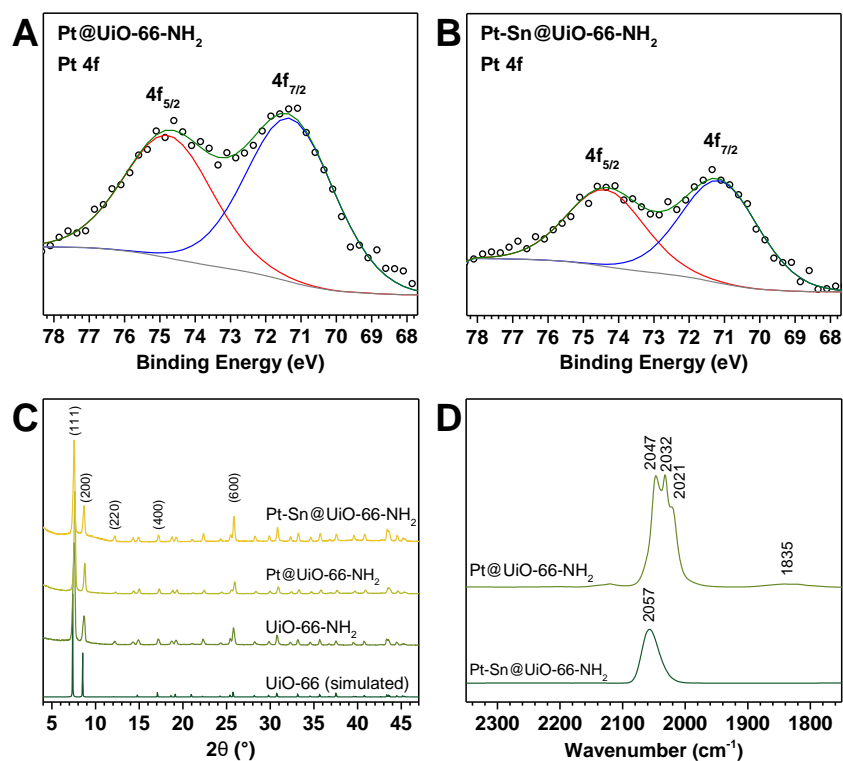
**Figure 3.** (A-B) Pt 4f XPS spectra of Pt@UiO-66-NH$_2$ and Pt-Sn@UiO-66-NH$_2$. (C) DRIFTS spectra of adsorbed CO on Pt@UiO-66-NH$_2$ and Pt-Sn@UiO-66-NH$_2$ at room temperature. (D) PXRD patterns of as-prepared UiO-66-NH$_2$, Pt@UiO-66-NH$_2$, and Pt-Sn@UiO-66-NH$_2$.

While XPS analysis provide the evidence of the formation of Pt-Sn bimetallic surface on the nanocluster encapsulated in UiO-66-NH$_2$, it is known that the presence of Sn in a surfactant-free nanocluster system is susceptible to oxidation.[33-34] This agrees with our XPS data analysis, where we observe the presence of both cationic Sn$^{2+}$ and metallic Sn. To further understand the electronic properties under a controlled condition that is more relevant to catalytic studies, we performed an in-situ diffuse reflectance infrared Fourier transform spectroscopy (DRIFTS) studies using CO as the probe molecule. Due to its high sensitivity to

the local bonding environment, and the electronic surface properties of the supported catalyst, CO has been widely used as the probe molecule.[35-37] Figure 3D shows the IR spectra of CO adsorbed at saturation coverage at room temperature on the Pt@UiO-66-NH$_2$ and Pt-Sn@UiO-66-NH$_2$. Prior to the CO adsorption studies, the catalysts were reduced in-situ under 10%H$_2$/He flow at 200 °C, and further cooled to room temperature under He flow. Upon saturation of CO on the surface of Pt@UiO-66-NH$_2$¸we observed vibrational bands of CO linearly adsorbed on Pt at the 2020 – 2047 cm$^{-1}$ range, and a bridge CO vibration band at 1835 cm$^{-1}$. Upon formation of PtSn surface, only a single vibration band of adsorbed CO is observed at 2057 cm$^{-1}$. This CO vibration peak shift to higher energy suggests the electron localization from Pt to Sn, and thus less electron is donated to the CO π* anti-bonding orbital.[38] Similar blue shift in CO adsorption has also been observed in Pt-Sn system upon alloying of Sn, which was could be attributed to the size effect.[39] As shown from our TEM analysis previously, the size of the nanocluster increases from 1.4 to 1.6 nm upon addition of Sn. Noteworthy, the formation of Pt-Sn bimetallic surface effectively removed Pt-Pt bridge sites on the nanocluster surface for bridging CO adsorption (1835 cm$^{-1}$ peak in Figure 3D). To further verify the formation of Pt-Sn surface upon 200°C in-situ reduction treatment, we performed CO adsorption on samples treated at different temperatures. As shown in Figure S5, upon H$_2$/He treatment of the Sn impregnated samples at 100°C, most of the surface remain Pt-rich, as indicated by the CO adsorption stretching at 2047 cm$^{-1}$. However, upon reduction treatment at 200°C,[31-32] the peak shift to a higher wavenumber of 2057 cm$^{-1}$. In the absence of Pt, the CO does not adsorb on the Sn impregnated UiO-66-NH$_2$ even after 200°C treatment in 10%H$_2$/He atmosphere (Figure S5).

In addition, we used variable-temperature DRIFTS and measured the temperature-dependent desorption of CO, which suggests that CO molecules adsorb exclusively on isolated Pt sites on the Pt-Sn surface of the encapsulated nanocluster. Figure 4A shows that upon desorption of CO from the Pt nanoclusters surface, the CO vibrational band red-shifted from 2047 to 2023 cm$^{-1}$. The coverage dependent shift is commonly observed on monometallic Pt surface, correlated to changes in dipole-dipole coupling between adsorbed CO molecules on the Pt surface.[40-42] Upon desorption of CO from the monometallic Pt surface at elevated temperature, the CO coverage on the surface decreases, thus minimizing the coupling between adjacently adsorbed CO molecules. However, due to the dilution of Pt atoms on the Pt-Sn surfaces by Sn atoms, the adsorbed CO on the isolated Pt sites are spatially separated thus minimizing the dipole-dipole coupling between adjacent CO molecules. Upon desorption of CO from the Pt-Sn surface at elevated temperature, the vibration stretch of CO remains unshifted at 2057 cm$^{-1}$ (Figure 4B). This desorption behavior have recently been observed in isolated single atom Pt supported on both metal oxides and Pt-Cu alloy system.[35-36, 43]
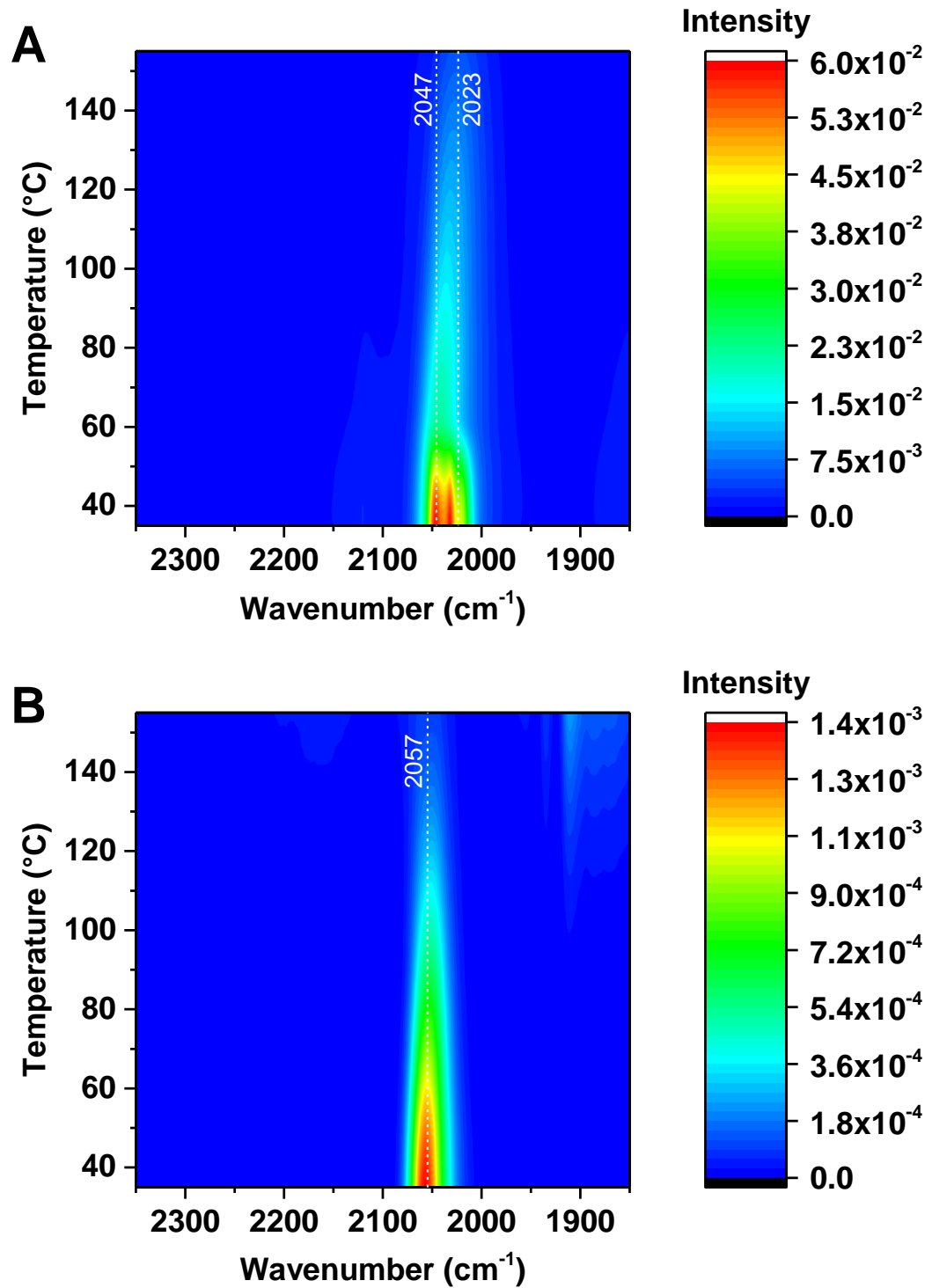
**Figure 4.** Temperature-dependent IR spectra of adsorbed CO on (A) Pt@UiO-66-NH₂ and (B)Pt-Sn@UiO-66-NH₂ under Helium flow in the range of 35 – 175 °C.

The isolated Pt sites on bimetallic surface was proposed to hinder the activation of C=C double bonds, and increases the activation of C=O bond, thus improving the selectivity of unsaturated aldehydes hydrogenation.[9] Figure S6, shows that upon introduction of Sn, the Pt-Sn@UiO-66-NH$_2$ catalyst shows significantly improved selectivity towards furfuryl alcohol (93%) in vapor phase furfural hydrogenation.. In contrast, the monometallic Pt nanocluster encapsulated in UiO-66-NH$_2$only shows a selectivity of 55% with the furan as the minor product.

In summary, we prepared Pt-Sn nanocluster confined inside the pores in UiO-66-NH$_2$. The formation of Pt-Sn bimetallic surface of nanocluster was probed using in-situ IR spectroscopic studies of CO adsorption and temperature-programmed desorption, in complementary to other techniques such as HAADF-STEM and XPS analysis. IR studies using surface sensitive probe molecule such as CO indicated the formation of Pt-Sn interface that shows a different electronic surface property compare to the monometallic Pt. Furthermore, CO desorption studies using variable-temperature IR indicates that the Pt atoms on the Pt-Sn surface are spatially isolated compare to monometallic Pt surface, thus provide direct evidence of Pt-Sn interface formation. A facile and efficient strategy to synthesize bimetallic nanocluster encapsulated through impregnation is shown as a promising catalyst for the selective hydrogenation of furfural to an industry-relevant commodity chemical, furfuryl alcohol.

**3.8 Supporting Information**
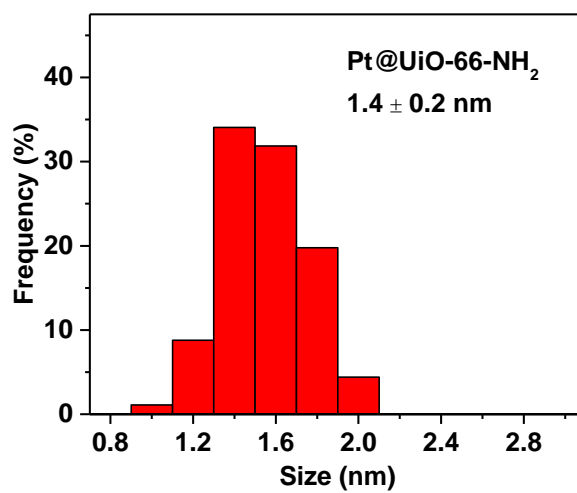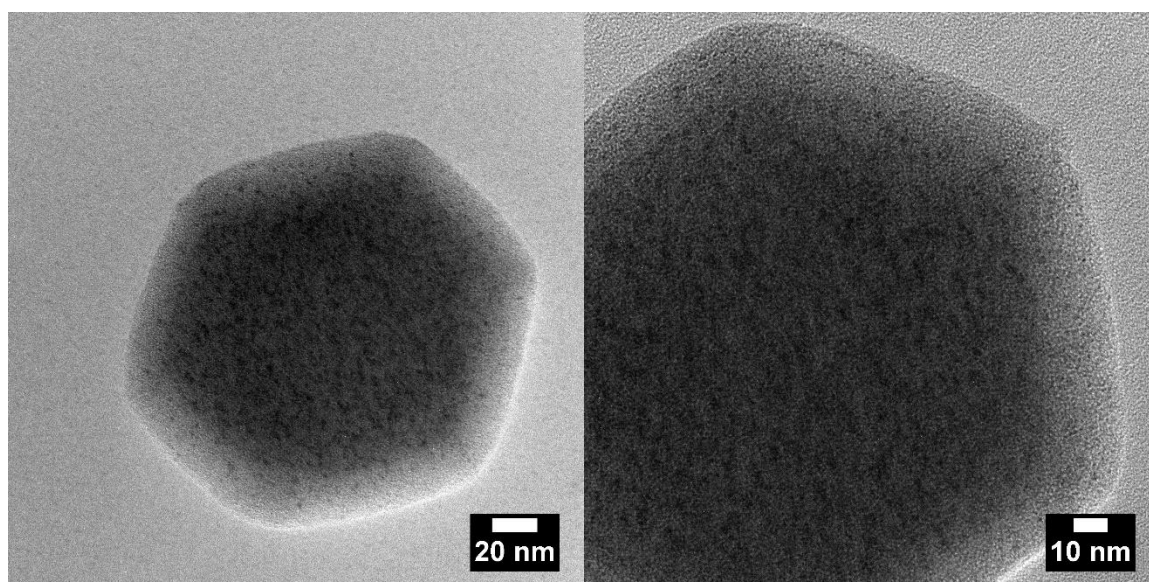


**Figure S1.** TEM images of Pt@UiO-66-NH$_2$ and the nanocluster size distribution.
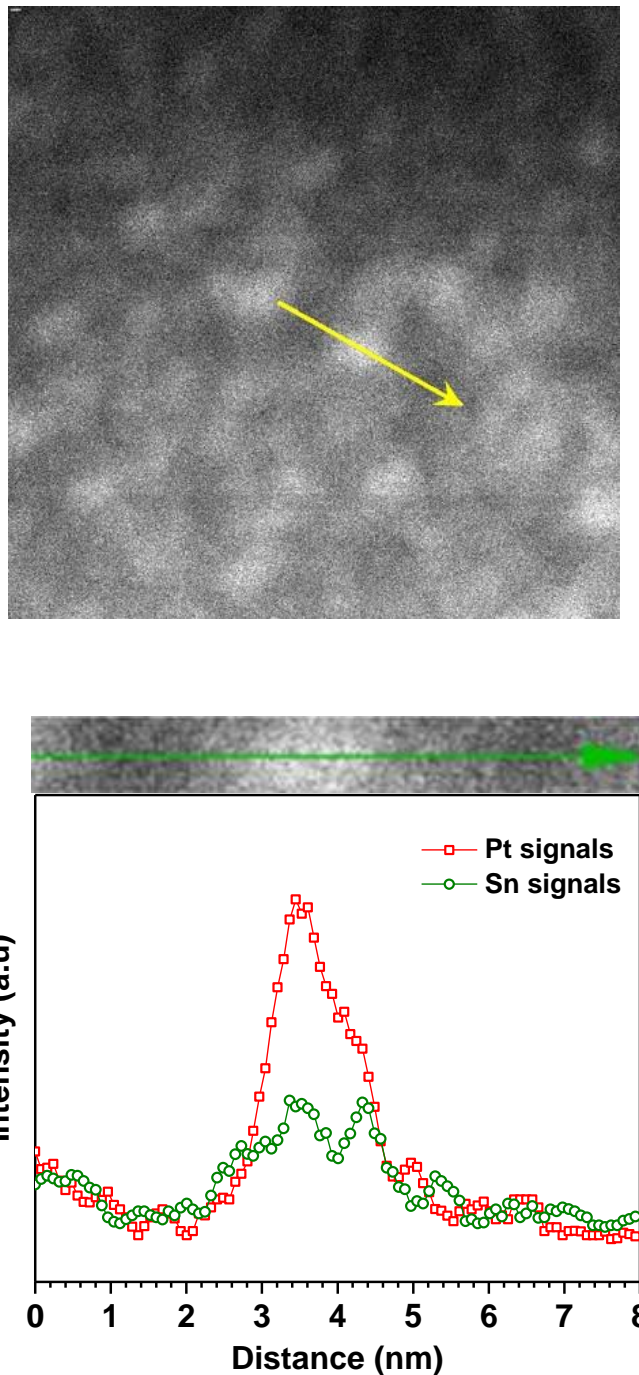
**Figure S2.** (Top) HAADF-STEM image of representative Pt-Sn@UiO-66-NH$_2$ nanocluster. The yellow arrow (8 nm in length) indicates the region of EDS line scan was obtained. (Bottom) The EDS line scans of representative Pt-Sn@UiO-66-NH$_2$ nanocluster. The red square and green circles are Pt and Sn signals of Pt and Sn respectively.
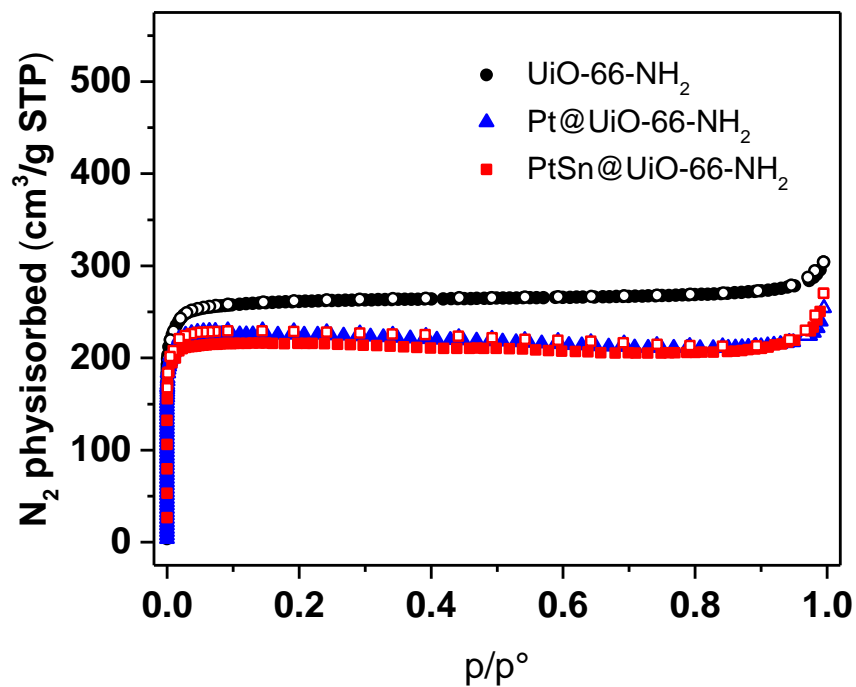
**Figure S3.** N$_2$ physisorption at 77 K to determine the isotherm of UiO-66-NH$_2$, Pt@UiO-66-NH$_2$, and Pt-Sn@UiO-66-NH$_2$

**Table S1.** BET surface area determined from isotherm from p/p° 0.01-0.1

| **Samples** | **BET Surface area (m$^2$/g)** |
|---|---|
| **UiO-66-NH$_2$** | 1027 |
| **Pt@UiO-66-NH$_2$** | 932 |
| **Pt-Sn@UiO-66-NH$_2$** | 891 |
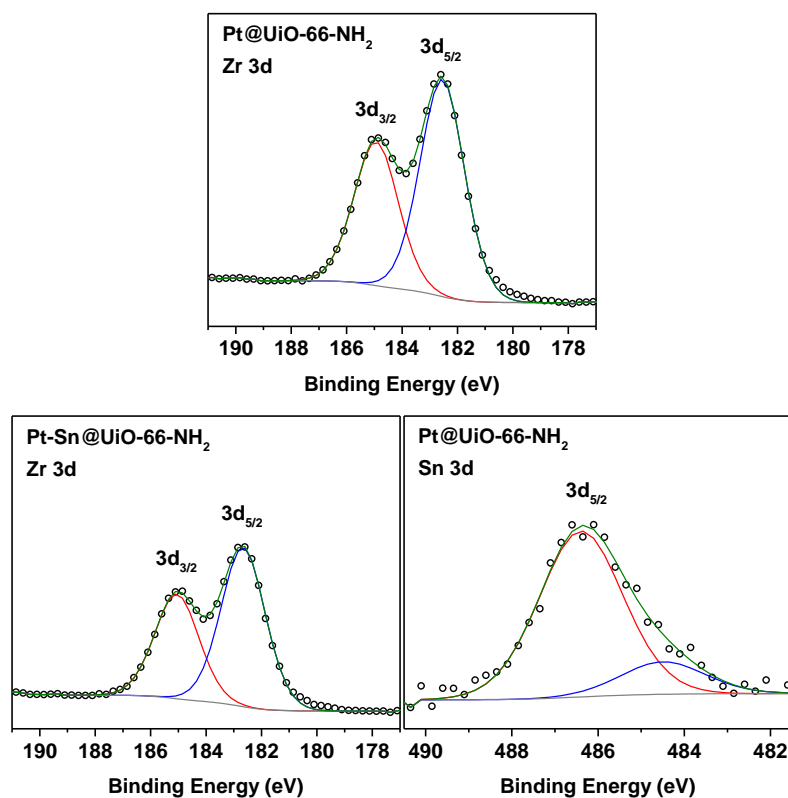
**Figure S4.** X-ray photoelectron spectroscopy analysis of Zr and Sn in UiO-66-NH2 metal-organic frameworks.

**Table S2.** Deconvoluted peak of XPS spectra of Zr 3d, Pt 4f and Sn 3d regions.

| Samples | $Zr^{4+}$ $3d_{5/2}$ (eV) | $Pt^0$ $4f_{7/2}$ (eV) | $Pt^0$ $4f_{7/2}$ (area) | $Sn^0$ $3d_{5/2}$ (eV) | $Sn^0$ $3d_{5/2}$ (area) | $Sn^{(2+,4+)}$ $3d_{5/2}$ (eV) | $Sn^{(2+,4+)}$ $3d_{5/2}$ (area) |
|---|---|---|---|---|---|---|---|
| **Pt@UiO-66-NH₂** | 182.5 | 71.3 | 454.6 | - | - | - | - |
| **Pt-Sn@UiO-66-NH₂** | 182.6 | 71.2 | 313.1 | 484.4 | 159.3 | 486.3 | 813.4 |

All XPS spectra were carefully calibrated based on the standard binding energy of C(sp2) at

284.6 eV. Both Pt and Sn peak area was normalized with respect to the peak area of Zr 3d5/2

(a.u. 16298.5).
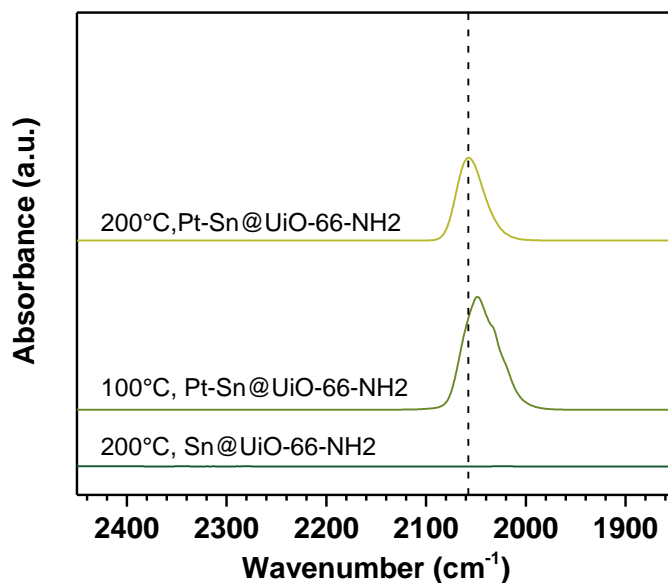
**Figure S5.** IR spectroscopy of adsorbed CO on Pt-Sn@UiO-66-NH$_2$ and Sn@UiO-66-NH upon in-situ reduction at different temperature under 10%H$_2$/He flow.



**Figure S6.** Catalytic performance of furfural hydrogenation at 160 °C for Pt@UiO-66-NH$_2$ and Pt-Sn@UiO-66-NH$_2$. Condition: Furfural = 0.023 mL/min, H$_2$ =11.4 mL, He = 8.4 mL/min, 160 °C, 5 mg catalyst (0.21 mg Pt).

## 3.9 References

(1)     Lange, J.-P.; van der Heide, E.; van Buijtenen, J.; Price, R. Furfural—A Promising Platform for Lignocellulosic Biofuels. *ChemSusChem* 2012, *5* (1), 150-166, DOI: doi:10.1002/cssc.201100648.
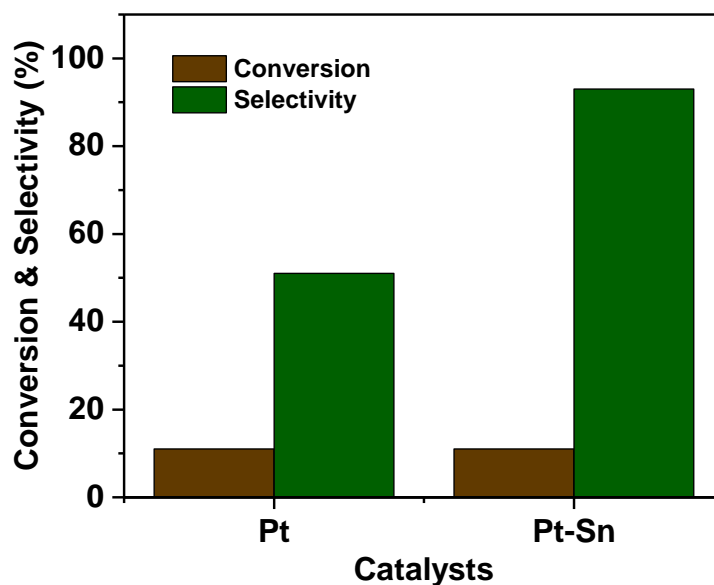
(2)     Mariscal, R.; Maireles-Torres, P.; Ojeda, M.; Sádaba, I.; López Granados, M. Furfural: a renewable and versatile platform molecule for the synthesis of chemicals and fuels. *Energy & Environmental Science* 2016, *9* (4), 1144-1189, DOI: 10.1039/C5EE02666K.

(3)     Mamman, A. S.; Lee, J.-M.; Kim, Y.-C.; Hwang, I. T.; Park, N.-J.; Hwang, Y. K.; Chang, J.-S.; Hwang, J.-S. Furfural: Hemicellulose/xylosederived biochemical. *Biofuels, Bioproducts and Biorefining* 2008, *2* (5), 438-454, DOI: 10.1002/bbb.95.

(4)     Mohr, C.; Claus, P. Hydrogenation properties of supported nanosized gold particles. *Science Progress* 2001, *84* (4), 311-334, DOI: 10.3184/003685001783238925.

(5)     Kliewer, C. J.; Bieri, M.; Somorjai, G. A. Hydrogenation of the α,β-Unsaturated Aldehydes Acrolein, Crotonaldehyde, and Prenal over Pt Single Crystals: A Kinetic and Sum-Frequency Generation Vibrational Spectroscopy Study. *J. Am. Chem. Soc.* 2009, *131* (29), 9958-9966, DOI: 10.1021/ja8092532.

(6)     Rao, R.; Dandekar, A.; Baker, R. T. K.; Vannice, M. A. Properties of Copper Chromite Catalysts in Hydrogenation Reactions. *J. Catal.* 1997, *171* (2), 406-419, DOI: 10.1006/jcat.1997.1832.

(7)     Katz, S. A.; Salem, H. The toxicology of chromium with respect to its chemical speciation: A review. *J. Appl. Toxicol.* 1993, *13* (3), 217-224, DOI: 10.1002/jat.2550130314.

(8)     Mäki-Arvela, P.; Hájek, J.; Salmi, T.; Murzin, D. Y. Chemoselective hydrogenation of carbonyl compounds over heterogeneous catalysts. *Appl. Catal. A* 2005, *292*, 1-49, DOI: 10.1016/j.apcata.2005.05.045.

(9)     Gallezot, P.; Richard, D. Selective Hydrogenation of α,β-Unsaturated Aldehydes. *Catalysis Reviews* 1998, *40* (1-2), 81-126, DOI: 10.1080/01614949808007106.

(10)    Corma, A.; Serna, P. Chemoselective Hydrogenation of Nitro Compounds with Supported Gold Catalysts. *Science* 2006, *313* (5785), 332-334, DOI: 10.1126/science.1128383.

(11)    Fu, Q.; Li, W.-X.; Yao, Y.; Liu, H.; Su, H.-Y.; Ma, D.; Gu, X.-K.; Chen, L.; Wang, Z.; Zhang, H.; Wang, B.; Bao, X. Interface-Confined Ferrous Centers for Catalytic Oxidation. *Science* 2010, *328* (5982), 1141-1144, DOI: 10.1126/science.1188267.


(12)    Zhao, M.; Yuan, K.; Wang, Y.; Li, G.; Guo, J.; Gu, L.; Hu, W.; Zhao, H.; Tang, Z. Metal–organic frameworks as selectivity regulators for hydrogenation reactions. *Nature* 2016, *539*, 76, DOI: 10.1038/nature19763.


(13)    Yuan, K.; Song, T.; Wang, D.; Zhang, X.; Gao, X.; Zou, Y.; Dong, H.; Tang, Z.; Hu, W. Effective and Selective Catalysts for Cinnamaldehyde Hydrogenation: Hydrophobic Hybrids of Metal–Organic Frameworks, Metal Nanoparticles, and Micro- and Mesoporous Polymers. *Angew. Chem. Int. Ed.* 2018, *57* (20), 5708-5713, DOI: 10.1002/anie.201801289.


(14)    Kobayashi, T.; Perras, F. A.; Goh, T. W.; Metz, T. L.; Huang, W.; Pruski, M. DNP-Enhanced Ultrawideline Solid-State NMR Spectroscopy: Studies of Platinum in Metal-Organic Frameworks. *J Phys Chem Lett* 2016, *7* (13), 2322-7, DOI: 10.1021/acs.jpclett.6b00860.


(15)    Xiao, C.; Goh, T. W.; Brashler, K.; Pei, Y.; Guo, Z.; Huang, W. In situ X-ray absorption spectroscopy studies of kinetic interaction between platinum(II) ions and UiO-66 series metal-organic frameworks. *J. Phys. Chem. B* 2014, *118* (49), 14168-76, DOI: 10.1021/jp5066456.


(16)    Guo, Z. Y.; Xiao, C. X.; Maligal-Ganesh, R. V.; Zhou, L.; Goh, T. W.; Li, X. L.; Tesfagaber, D.; Thiel, A.; Huang, W. Y. Pt Nanoclusters Confined within Metal Organic Framework Cavities for Chemoselective Cinnamaldehyde Hydrogenation. *ACS Catal.* 2014, *4* (5), 1340-1348, DOI: 10.1021/cs400982n.


(17)    Liu, J. Aberration-corrected scanning transmission electron microscopy in single-atom catalysis: Probing the catalytically active centers. *Chin. J. Catal.* 2017, *38* (9), 1460-1472, DOI: 10.1016/S1872-2067(17)62900-0.


(18)    Chen, L.; Luque, R.; Li, Y. Controllable design of tunable nanostructures inside metal–organic frameworks. *Chem. Soc. Rev.* 2017, *46* (15), 4614-4630, DOI: 10.1039/C6CS00537C.


(19)    Chen, L.; Luque, R.; Li, Y. Encapsulation of metal nanostructures into metal–organic frameworks. *Dalton Trans.* 2018, *47* (11), 3663-3668, DOI: 10.1039/C8DT00092A.

(20)    Aijaz, A.; Karkamkar, A.; Choi, Y. J.; Tsumori, N.; Rönnebro, E.; Autrey, T.; Shioyama, H.; Xu, Q. Immobilizing Highly Catalytically Active Pt Nanoparticles inside the Pores of Metal–Organic Framework: A Double Solvents Approach. *J. Am. Chem. Soc.* 2012, *134* (34), 13926-13929, DOI: 10.1021/ja3043905.

(21)    Chen, L.; Chen, H.; Luque, R.; Li, Y. Metal−organic framework encapsulated Pd nanoparticles: towards advanced heterogeneous catalysts. *Chem. Sci.* 2014, *5* (10), 3708-3714, DOI: 10.1039/C4SC01847H.

(22)    Chen, L.; Huang, B.; Qiu, X.; Wang, X.; Luque, R.; Li, Y. Seed-mediated growth of MOF-encapsulated Pd@Ag core–shell nanoparticles: toward advanced room temperature nanocatalysts. *Chem. Sci.* 2016, *7* (1), 228-233, DOI: 10.1039/C5SC02925B.

(23)    Li, X. L.; Guo, Z. Y.; Xiao, C. X.; Goh, T. W.; Tesfagaber, D.; Huang, W. Y. Tandem Catalysis by Palladium Nanoclusters Encapsulated in Metal-Organic Frameworks. *ACS Catal.* 2014, *4* (10), 3490-3497, DOI: 10.1021/cs5006635.

(24)    Guo, Z. Y.; Kobayashi, T.; Wang, L. L.; Goh, T. W.; Xiao, C. X.; Caporini, M. A.; Rosay, M.; Johnson, D. D.; Pruski, M.; Huang, W. Y. Selective Host-Guest Interaction between Metal Ions and Metal-Organic Frameworks Using Dynamic Nuclear Polarization Enhanced Solid-State NMR Spectroscopy. *Chem. Eur. J.* 2014, *20* (49), 16308-16313, DOI: 10.1002/chem.201403884.

(25)    Yuan, S.; Feng, L.; Wang, K.; Pang, J.; Bosch, M.; Lollar, C.; Sun, Y.; Qin, J.; Yang, X.; Zhang, P.; Wang, Q.; Zou, L.; Zhang, Y.; Zhang, L.; Fang, Y.; Li, J.; Zhou, H.-C. Stable Metal–Organic Frameworks: Design, Synthesis, and Applications. *Adv. Mater.* 2018, *30* (37), 1704303, DOI: 10.1002/adma.201704303.

(26)    Qin, J.-S.; Yuan, S.; Lollar, C.; Pang, J.; Alsalme, A.; Zhou, H.-C. Stable metal–organic frameworks as a host platform for catalysis and biomimetics. *Chem. Commun.* 2018, *54* (34), 4231-4249, DOI: 10.1039/C7CC09173G.

(27)    Wang, W.-W.; Du, P.-P.; Zou, S.-H.; He, H.-Y.; Wang, R.-X.; Jin, Z.; Shi, S.; Huang, Y.-Y.; Si, R.; Song, Q.-S.; Jia, C.-J.; Yan, C.-H. Highly Dispersed Copper Oxide Clusters as Active Species in Copper-Ceria Catalyst for Preferential Oxidation of Carbon Monoxide. *ACS Catal.* 2015, *5* (4), 2088-2099, DOI: 10.1021/cs5014909.

(28)    Bai, Y.; Dou, Y.; Xie, L.-H.; Rutledge, W.; Li, J.-R.; Zhou, H.-C. Zr-based metal-organic frameworks: design, synthesis, structure, and applications. *Chem. Soc. Rev.* 2016, *45* (8), 2327-2367, DOI: 10.1039/C5CS00837A.

(29)    Pennycook, S. J.; Jesson, D. E. High-resolution Z-contrast imaging of crystals. *Ultramicroscopy* 1991, *37* (1), 14-38, DOI: 10.1016/0304-3991(91)90004-P.

(30)    Ramos-Fernandez, E. V.; Pieters, C.; van der Linden, B.; Juan-Alcañiz, J.; Serra-Crespo, P.; Verhoeven, M. W. G. M.; Niemantsverdriet, H.; Gascon, J.; Kapteijn, F. Highly dispersed platinum in metal organic framework NH2-MIL-101(Al) containing phosphotungstic acid – Characterization and catalytic performance. *J. Catal.* 2012, *289*, 42-52, DOI: 10.1016/j.jcat.2012.01.013.

(31)    Sharma, L. D.; Kumar, M.; Saxena, A. K.; Rawat, D. S.; Prasada Rao, T. S. R. The determination of accessible Pt metal fraction in Pt–Sn/Al2O3 reforming catalyst. *Appl. Catal. A* 1998, *168* (2), 251-259, DOI: 10.1016/S0926-860X(97)00356-6.

(32)    da Silva, A. B.; Jordão, E.; Mendes, M. J.; Fouilloux, P. Effect of metal-support interaction during selective hydrogenation of cinnamaldehyde to cinnamyl alcohol on platinum based bimetallic catalysts. *Appl. Catal. A* 1997, *148* (2), 253-264, DOI: 10.1016/S0926-860X(96)00102-0.

(33)    Du, W.; Yang, G.; Wong, E.; Deskins, N. A.; Frenkel, A. I.; Su, D.; Teng, X. Platinum-Tin Oxide Core–Shell Catalysts for Efficient Electro-Oxidation of Ethanol. *J. Am. Chem. Soc.* 2014, *136* (31), 10862-10865, DOI: 10.1021/ja505456w.

(34)    Du, W.; Wang, Q.; Saxner, D.; Deskins, N. A.; Su, D.; Krzanowski, J. E.; Frenkel, A. I.; Teng, X. Highly Active Iridium/Iridium–Tin/Tin Oxide Heterogeneous Nanoparticles as Alternative Electrocatalysts for the Ethanol Oxidation Reaction. *J. Am. Chem. Soc.* 2011, *133* (38), 15172-15183, DOI: 10.1021/ja205649z.

(35)    Ding, K.; Gulec, A.; Johnson, A. M.; Schweitzer, N. M.; Stucky, G. D.; Marks, L. D.; Stair, P. C. Identification of active sites in CO oxidation and water-gas shift over supported Pt catalysts. *Science* 2015, *350* (6257), 189-192, DOI: 10.1126/science.aac6368.

(36)    Jones, J.; Xiong, H.; DeLaRiva, A. T.; Peterson, E. J.; Pham, H.; Challa, S. R.; Qi, G.; Oh, S.; Wiebenga, M. H.; Pereira Hernández, X. I.; Wang, Y.; Datye, A. K. Thermally stable single-atom platinum-on-ceria catalysts via atom trapping. *Science* 2016, *353* (6295), 150-154, DOI: 10.1126/science.aaf8800.

(37)    DeRita, L.; Dai, S.; Lopez-Zepeda, K.; Pham, N.; Graham, G. W.; Pan, X.; Christopher, P. Catalyst Architecture for Stable Single Atom Dispersion Enables Site-Specific Spectroscopic and Reactivity Measurements of CO Adsorbed to Pt Atoms, Oxidized Pt Clusters, and Metallic Pt Clusters on TiO2. *J. Am. Chem. Soc.* 2017, *139* (40), 14150-14165, DOI: 10.1021/jacs.7b07093.

(38)    Schubert, M. M.; Kahlich, M. J.; Feldmeyer, G.; Hüttner, M.; Hackenberg, S.; Gasteiger, H. A.; Behm, R. J. Bimetallic PtSn catalyst for selective CO oxidation in H2-rich gases at low temperatures. *Phys. Chem. Chem. Phys.* 2001, *3* (6), 1123-1131, DOI: 10.1039/B008062O.

(39)    Balakrishnan, K.; Schwank, J. FTIR study of bimetallic Pt-Sn/Al2O3 catalysts. *J. Catal.* 1992, *138* (2), 491-499, DOI: doi.org/10.1016/0021-9517(92)90301-W.

(40)    Crossley, A.; King, D. A. Infrared spectra for co isotopes chemisorbed on Pt "111": Evidence for strong absorbate coupling interactions. *Surf. Sci.* 1977, *68*, 528-538, DOI: 10.1016/0039-6028(77)90245-X.

(41)    Allian, A. D.; Takanabe, K.; Fujdala, K. L.; Hao, X.; Truex, T. J.; Cai, J.; Buda, C.; Neurock, M.; Iglesia, E. Chemisorption of CO and Mechanism of CO Oxidation on Supported Platinum Nanoclusters. *J. Am. Chem. Soc.* 2011, *133* (12), 4498-4517, DOI: 10.1021/ja110073u.

(42)    Zhang, Q.; Lee, I.; Ge, J.; Zaera, F.; Yin, Y. Surface-Protected Etching of Mesoporous Oxide Shells for the Stabilization of Metal Nanocatalysts. *Adv. Funct. Mater.* 2010, *20* (14), 2201-2214, DOI: 10.1002/adfm.201000428.

(43)    Marcinkowski, M. D.; Darby, M. T.; Liu, J.; Wimble, J. M.; Lucci, F. R.; Lee, S.; Michaelides, A.; Flytzani-Stephanopoulos, M.; Stamatakis, M.; Sykes, E. C. H. Pt/Cu single-atom alloys as coke-resistant catalysts for efficient C–H activation. *Nature Chem.* 2018, *10*, 325, DOI: 10.1038/nchem.2915.

# CHAPTER 4.   IN-SITU DRIFTS STUDIES OF THERMALLY STABLE ISOLATED SINGLE PT ATOM IN N-DOPED METAL-ORGANIC FRAMEWORK

*Manuscript submitted*

Tian Wei Goh, Takeshi Kobayashi, Prof. Marek Pruski, Prof. Wenyu Huang

## 4.1 Abstract

Accessible metal-sites that allow the adsorption of substrate plays an essential role in many catalytic applications. In heterogeneous catalyst, to achieve maximum dispersion of accessible surface metals atom is by stabilizing the single-atom on various high surface area support. The highly ordered arrangement of organic linkers and metal-oxo nodes in a crystalline metal-organic frameworks (MOFs) make them an ideal platform in designing motif to stabilize single atom-metal sites. By using in-situ diffuse reflectance infrared spectroscopy (DRIFTS) with CO chemisorption, we were able to identify the isolate Pt active sites in N-doped MOFs for application in CO oxidation. The isolated single Pt atom sites was further confirmed by aberration corrected scanning transmission electron microscopy (STEM) and spectroscopy techniques such as X-ray Photoelectron Spectroscopy (XPS), dynamic nuclear polarization (DNP) enhanced $^{195}$Pt solid-state NMR (ssNMR)

## 4.2 Discussion

In recent years, many promising heterogeneous catalysts have been developed, and extensively investigated for clean energy technologies such as hydrogen production, solar energy conversion, and $CO_2$ reduction.[1-6] The new frontier of heterogeneous catalyst driven

by the advancement of characterization tools and affordable computing power has promoted the exploration and development of atomically dispersed single-atom catalyst (SAC). Isolated single-atom supported on high surface area, and robust materials such as metal oxides, zeolites, metal-organic frameworks (MOFs), and carbon-based materials presents a maximum atomic efficiency and new catalytic properties due to it distinct electronic properties.[7-11]

Three-dimensional crystalline materials such as MOFs constructed from organic linker and inorganic secondary building units has become an emerging platform for heterogeneous single-metal-site catalysts due to the flexibility in MOFs assembly.[9-11] The modular assembly of MOF components lead to a highly tunable structure with well-defined pore geometry, high surface area, and facile chemical functionalization, thus allowing the formation of a relatively uniform catalytic active sites.[12-15] Recent years, Lin et. al. has developed isolated single atom catalyst using N-doped organic linker to stabilize transition metals such as Ru, Re, Ir, Pd, Co, and Fe for various organic transformation. [16-20] Isolated single Pt atoms on similar N-doped metal-organic framework has shown to be a promising catalyst for hydrogen production by water splitting.[3, 21-22] Understanding of the structure of the isolated single-atom catalyst is essential to understand the origins of the novel catalytic properties, the stability, and to further improve the rational design of the catalyst. Achieving this level of understanding requires advance characterization techniques such as aberration-corrected microscopy, X-ray absorption spectroscopy (XAS) and in-situ spectroscopy techniques to probe the local coordination of the isolated metal active sites.[21, 23-26]

The exclusive presence of single atom sites drawn from a technique such as high angle annular dark field scanning transmission electron microscopy (HAADF-STEM) provides statistically limited information, due to the analysis of a limited percentage of the overall sample.[27] Furthermore, identification of the isolated single atom through contrast difference remain challenging for the low Z transition metal, as the resulting displayed intensity is approximately proportional to the square of atomic number.[28-29] Moreover, many of the chemical properties of the single site catalyst are related to the electronic characteristics, which are challenging to determine through imaging methods.

Surface-sensitive techniques such as chemisorption of probe molecules on supported noble metal catalysts coupled with in-situ infrared (IR) spectroscopy is widely used to provide atomic and electronic structures of the surface binding sites. Thus, allow the direct observation of the catalytic active sites at ambient pressure, and provide statistically acceptable information on the identification and quantification of the specific active sites, would make valuable progress in the understanding of the single site structure. In-situ IR spectroscopy has been used extensively to investigate the stability and local electronic properties of the isolated single Pt atoms supported on various metal oxides such as $CeO_2$, $TiO_2$, $Cu_2O$, and $FeO_x$.[24-25, 30-32] Besides isolated single Pt atoms on metal oxides surface, in-situ CO-FTIR has also been shown to be practical in resolving isolated noble metal atoms on bimetallic alloy surfaces.[33-35] However, there is a very limited report on IR spectroscopic studies on isolated single atoms on carbon-based material, although supported single-site atom on carbon-based material has been widely used in electrochemistry and $H_2$ production reaction due to its conductivity nature.[22, 36-39] This is likely due to the strong absorbance of

carbon-based material which causes studies using diffuse reflectance infrared Fourier transform spectroscopy (DRIFTS) challenging.[40]

In this study, we investigated the electronic properties and stability of the isolated Pt single atom supported on the N-doped organic linker in the MOFs which is analogous to the isolated Pt supported on carbon and N-doped carbon using in-situ DRIFTS and CO as the probe molecules. The isolated single Pt atoms supported on MOF has shown exceptional stability at elevated temperature under both inert and oxidative atmosphere. The homogeneity of the isolated Pt sites in the crystalline MOFs' architecture provides a scaffold for a much straight forward fundamental surface chemistry studies at the atomic-level using IR spectroscopy. The isolated single site Pt was further confirmed by aberration-corrected scanning transmission electron microscopy (ac-STEM), ultrawideline dynamic nuclear polarization (DNP)-enhanced $^{195}$Pt solid-state nuclear magnetic resonance (ssNMR), and the oxidation state of the Pt was further confirmed by X-ray photoelectron spectroscopy (XPS).
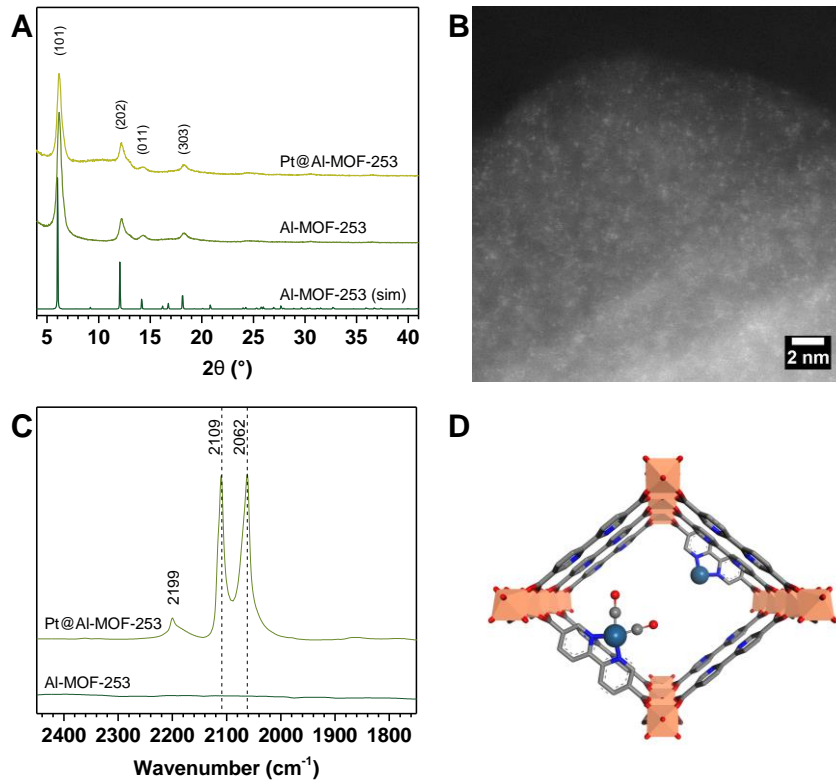
**Figure 1.** (A) PXRD patterns of MOF-253 indicates the crystallinity of the MOFs before and after incorporation of single Pt atoms. (B) HAADF-STEM image showing well-dispersed isolated single atom Pt (bright spots) supported on MOF-253. (C) IR spectra of CO adsorbed at 30 °C on Pt/MOF-253 (D) Model structure of CO adsorbed on Pt@MOF-253. Orange octahedron represents Al atoms, while green, blue, black, red represent Pt, N, C and O atoms respectively. H atoms are omitted for clarity.

We chose MOF-253 as the support to immobilize single atom due to the availability of the uncoordinated bipyridine for metal insertion, besides it's high thermal stability up to 350 °C.[41] MOF-253 which made up from the assembly of Al(OH) secondary building unit connected by 2,2'-bipyridine-5,5'-dicarboxylate was synthesized using solvothermal method based on the reported literature.[41] Furthermore, the isolated Pt supported on this N-doped

organic motif has been proven to be active for visible light photocatalytic $H_2$ production reaction from water splitting.[3, 22] The obtained white solid was further refluxed in acetonitrile in the presence of $Pt(DMSO)_2Cl_2$ for 16 hrs. The yellow solid powder was isolated and reduced under $10\%H_2/Ar$ at 300°C for 2 hours. The crystallinity of the obtained solid, and the stability of the framework upon Pt insertion was confirmed by powder X-ray diffraction (PXRD) pattern analysis (Figure 1A). ICP-MS analysis of the yellow solids upon Pt insertion shows that the metal loading for Pt is 16 wt%. The insertion of Pt and existence of the isolated Pt single atoms was independently verified by aberration corrected HAADF-STEM (Figure 1B). HAADF detector allows the collection of Rutherford scattered electrons exclusively, thus heavy atoms such as Pt with higher intensity of scattered electrons appear to be brighter.
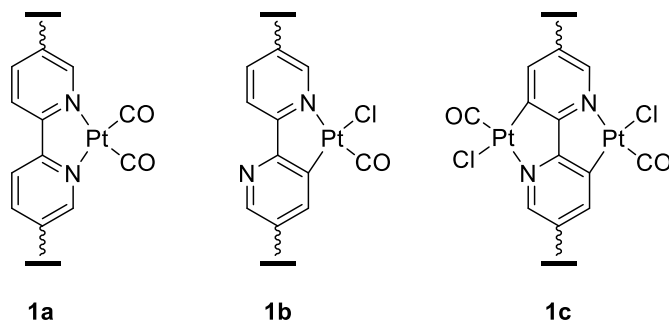


**Scheme 1.** CO adsorption on various isolated Pt complex.

Although at a high Pt loading of 16wt%, there is no observable Pt aggregation in the STEM imaging. The carboxylate organic linkers forming the MOF network upon coordination with metal-oxo nodes are known to able to spatially separate the isolated single atom thus inhibiting sintering.[42] Since, STEM imaging only provide a statistically limited information form a very small portion of the samples, we performed an extensive in-situ IR

spectroscopy studies to identify the local coordination and stability of the isolated single Pt site. About 10 mg of the bright yellow powder, Pt@MOF-253 was packed into a high-temperature sample chamber, and subject to 300 °C in-situ reduction under 10%$H_2$/He flow of 50 mL/min prior to the IR analysis. Upon cooling to 30 °C under He flow; a background spectrum was collected. After the in-situ pretreatment, CO was dosed into the chamber to saturation at 30 °C. The IR spectra of adsorbed CO on the Pt@MOF-253 (Figure 1C) reveal two narrow CO adsorption bands (FWHM = 12 $cm^{-1}$) at 2109 $cm^{-1}$ and 2062 $cm^{-1}$. These narrow IR bands can be attributed to the symmetric and asymmetric stretching of C-O in geminal dicarbonyl Pt as depicted in Scheme 1(1a).[43] For a single atom site adsorbed by two CO molecules forming a geminal dicarbonyl complex, the angle between two adsorbed carbonyl groups is related to the ratio of the IR peak areas of the symmetric and asymmetric stretches.[44-45] Based on the deconvoluted peak areas of these two bands (Figure Sx), the bond angle is estimated to be at 83° forming a distorted square planar complex. The other possible assignment for the 2109 $cm^{-1}$ and 2062 $cm^{-1}$ stretching vibration are the mononuclear (Scheme 1(1b)) and dinuclear platinum species (Scheme 1(1c)). [46-47] Under our experimental condition, the CO does not show any adsorption on MOF-253 in the absence of Pt. The CO band at 2199 $cm^{-1}$ is attributed to the $Pt^{\delta+}$ monocarbonyl because it's less redshifted from the gas phase vibration centered at 2143 $cm^{-1}$ due to the decreased Pt d-electron back donation to the CO $\pi^*$ antibonding orbital.[25, 48]

As proposed by literature, isolated single atom Pt on N-doped carbon or $C_3N_4$ are stabilized by the heteroatom N, which is analogous to the $Pt^0$ complex in Scheme 1(1a). However, this assignment remains ambiguous as most X-ray photoelectron spectroscopy

analysis indicates that the isolated Pt species is cationic in nature. Advance X-ray absorption studies (XAS) conclusively show the absence of Pt-Pt bonding, however, it is challenging to resolve between Pt-C and Pt-N bonding.[3, 22, 36-38] By monitoring the changes in C-O vibration of adsorbed CO under the operando condition, we were able to resolve the difference between the possible isolated single atom Pt species supported on N-doped carbon-based material. The intensity of the two vibration bands at 2109 and 2062 $cm^{-1}$ decreases gradually under both He and 20% O2/He flow as the temperature increases from 30 °C to 300 °C (Figure 2A-B). In both experiments, the peak intensity at 2062 $cm^{-1}$ decrease at a faster rate compared to the peak at 2109 $cm^{-1}$. Noteworthy, both the CO stretching bands do not show any observable coverage-dependent shift during the desorption process. These observations indicate that the CO was initially adsorbed on two independent spatially isolated Pt sites similar to the Scheme (1b and 1c), thus ruling out the possibility of geminal dicarbonyl Pt species (Scheme 1(1a)). The desorption of CO at surprisingly high temperature in both inert and oxidative atmosphere also indicates that the isolated Pt species has unprecedented stability at elevated temperature. No 2-fold bridge CO is observed up to 300 °C indicates that the isolated Pt sites in resistant towards CO-induced aggregation.

Given that the adsorbed CO on the isolated has very similar thermal and chemical stability under elevated He and O2 atmosphere. We attempted to probe the reactivity of the adsorbed CO using NO molecules. Both NO and CO are gases emitted from an internal combustion engine that are the major cause of $NO_x$ pollution in the world. These gases typically emitted during cold-start while the selective catalytic reduction catalyst in the catalytic converter is inactive.[49] In our operando DRIFTS studies, in the absence of oxygen,

the NO could form $NO^+$ by transferring electron to the cationic $Pt^{2+}$ to form $Pt^{\delta+}$.[43, 48] To our surprise, upon exposure to NO gas at 30 °C, the NO selectively substituted the CO adsorbed on the isolated Pt site as evident from Figure 2C. The rotational vibrational stretch of NO can be observed at around 1850 cm$^{-1}$. Additionally, vibrational stretch around 2400 cm$^{-1}$ possibly due to the formation of isocyanate N=C=O is observed. The introduction of NO could possibly reduce the $Pt^{2+}$ metal center as additional of switching back to CO gases does not regenerate the adsorption peak at 2062 cm$^{-1}$. Only P- and R- branch of the rotovibrational stretch is observed in Figure 2D, which can be easily removed upon flushing with He.
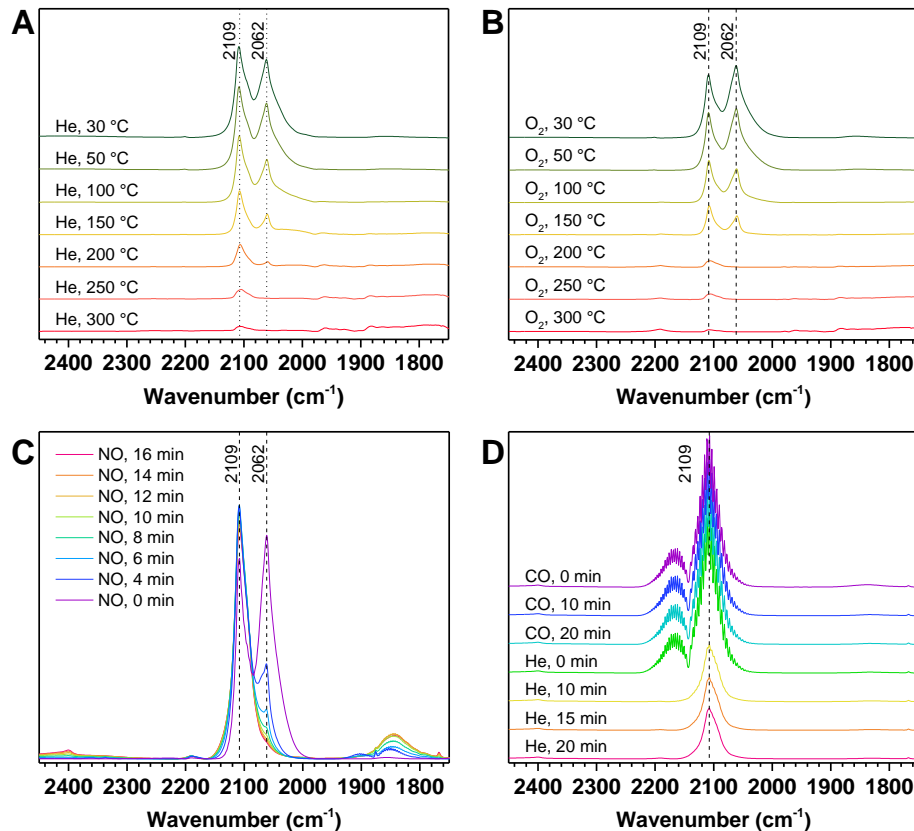


**Figure 2.** (A) Temperature-dependent IR of adsorbed CO on Pt@MOF-253 at 30 °C (B) Temperature-dependent IR of adsorbed CO from 30 °C to 300°C under dynamic He flow. (C) selective NO substitution on adsorbed CO at 30 °C. (D) Irreversible CO adsorption upon NO substitution.
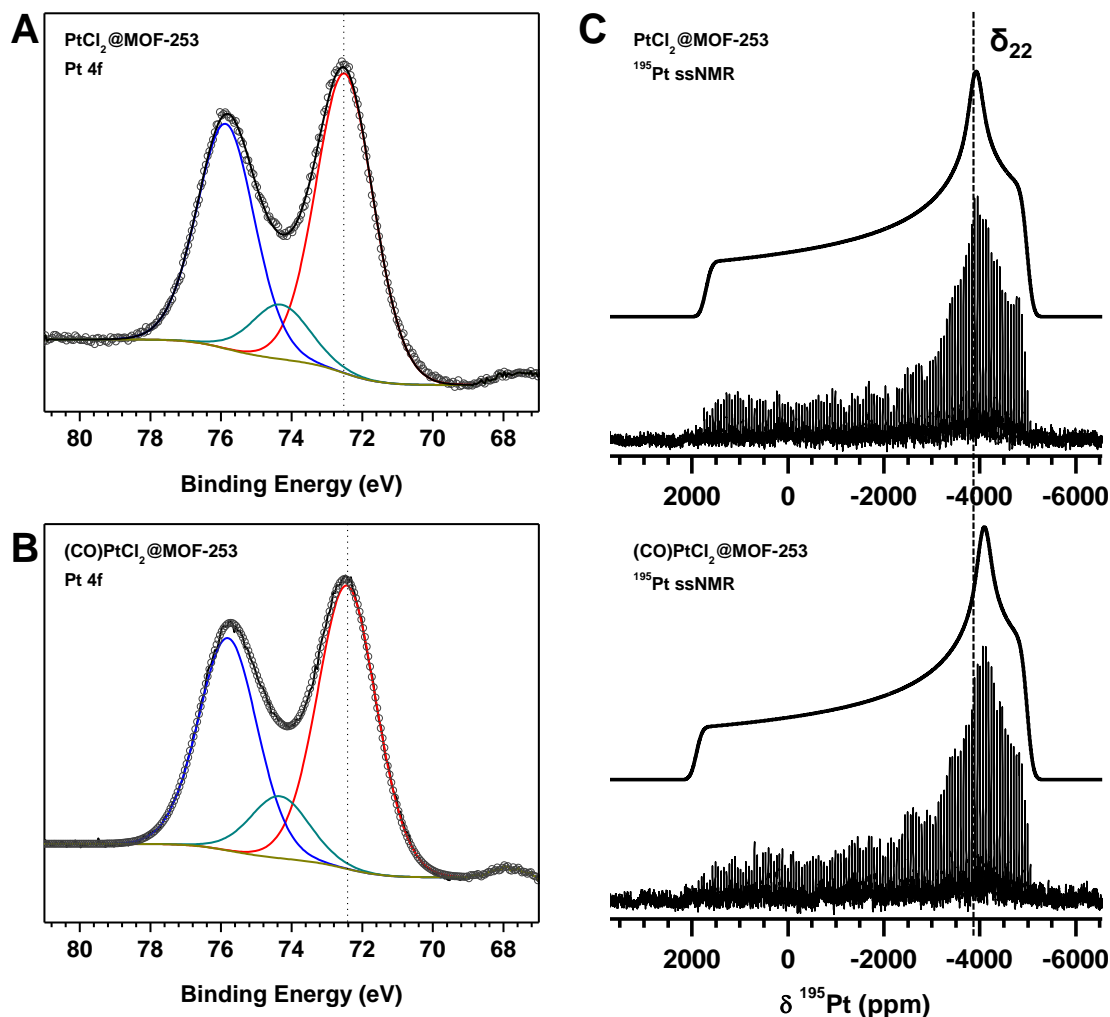
**Figure 3.** (A-B) Pt 4f XPS spectra of PtCl$_2$@MOF-253 and (CO)PtCl$_2$@MOF-253. (C) $^{195}$Pt solid state NMR of PtCl$_2$@MOF-253 and (CO)PtCl$_2$@MOF-253.

The oxidation state of the isolated Pt was evaluated by X-ray photoelectron spectroscopy (XPS) (Figure 3A-B). Upon coordination of PtCl$_2$(DMSO)$_2$ to the bipyridine linker, the Pt remain cationic as depicted in Figure 3A. The binding energy of the Pt 4f$_{5/2}$ of 75.0 eV indicates that the Pt is more likely to be in 2+ state. Upon H$_2$ treatment at 300°C followed by the CO adsorption, the Pt 4f$_{5/2}$ shifted by 0.2 eV to 74.8 eV, this shows that the Pt is

accepting more electrons from its local coordinated ligand. As shown in IR, the isolated Pt

upon reduction and CO chemisorption remain stable in air and elevated the temperature.

DNP-enhanced ultrawideline $^{195}$Pt[$^1$H] with BRAIN CP/WURST-CPMG (BCG) pulse

sequence as depicted in Figure 3C indicates that the isolated Pt is cis-coordinated to the

bipyridine linker of the MOF upon insertion of $PtCl_2(DMSO)_2$. Upon high-temperature

reduction and CO dosing, a slight chemical shift of the tensor $\delta_{22}$ from -3930 to -4100. This

unambiguously concludes that the Pt remain cis-coordinated to the bipyridine ligand as

depicted in Scheme 1(1b).

This study conclusively shown that isolated Pt supported on N-doped carbon-based

materials are thermally stable as it is stabilized by both heteroatom N and the C due to

rollover cyclometallation of the Pt. This model strongly supports the observation of isolated

cationic Pt probe by X-ray photoelectron spectroscopy and X-ray absorption spectroscopy.

Identifying the possible structure and local coordination of the isolate Pt active sites allow us

to formulate a better understanding of the mechanism of the $H_2$ production.

## 4.3 References

1.      Yamashita, H.; Mori, K.; Kuwahara, Y.; Kamegawa, T.; Wen, M.; Verma, P.; Che, M. Single-site and nano-confined photocatalysts designed in porous materials for environmental uses and solar fuels. *Chem. Soc. Rev.* **2018,** *47* (22), 8072-8096.

2.      Choi, K. M.; Kim, D.; Rungtaweevoranit, B.; Trickett, C. A.; Barmanbek, J. T. D.; Alshammari, A. S.; Yang, P.; Yaghi, O. M. Plasmon-Enhanced Photocatalytic CO2 Conversion within Metal–Organic Frameworks under Visible Light. *J. Am. Chem. Soc.* **2017,** *139* (1), 356-362.

3.      Zhou, T.; Du, Y.; Borgna, A.; Hong, J.; Wang, Y.; Han, J.; Zhang, W.; Xu, R. Post-synthesis modification of a metal–organic framework to construct a bifunctional photocatalyst for hydrogen production. *Enegy Environ. Sci.* **2013,** *6* (11), 3229-3234.

4.      Yang, X.; Sun, J.-K.; Kitta, M.; Pang, H.; Xu, Q. Encapsulating highly catalytically active metal nanoclusters inside porous organic cages. *Nat. Catal.* **2018,** *1* (3), 214-220.

5.      He, T.; Pachfule, P.; Wu, H.; Xu, Q.; Chen, P. Hydrogen carriers. *Nat. Rev. Mater.* **2016,** *1*, 16059.

6.      Wang, C.; deKrafft, K. E.; Lin, W. Pt Nanoparticles@Photoactive Metal–Organic Frameworks: Efficient Hydrogen Evolution via Synergistic Photoexcitation and Electron Injection. *J. Am. Chem. Soc.* **2012,** *134* (17), 7211-7214.

7.      Rivera-Cárcamo, C.; Serp, P. Single Atom Catalysts on Carbon-Based Materials. *ChemCatChem* **2018,** *10* (22), 5058-5091.

8.      Wang, A.; Li, J.; Zhang, T. Heterogeneous single-atom catalysis. *Nat. Rev. Chem.* **2018,** *2* (6), 65-81.

9.      Liang, Z.; Qu, C.; Xia, D.; Zou, R.; Xu, Q. Atomically Dispersed Metal Sites in MOF-Based Materials for Electrocatalytic and Photocatalytic Energy Conversion. *Angew. Chem. Int. Ed.* **2018,** *57* (31), 9604-9633.

10.     Rogge, S. M. J.; Bavykina, A.; Hajek, J.; Garcia, H.; Olivos-Suarez, A. I.; Sepúlveda-Escribano, A.; Vimont, A.; Clet, G.; Bazin, P.; Kapteijn, F.; Daturi, M.; Ramos-Fernandez, E. V.; Llabrés i Xamena, F. X.; Van Speybroeck, V.; Gascon, J. Metal–organic and covalent organic frameworks as single-site catalysts. *Chem. Soc. Rev.* **2017,** *46* (11), 3134-3184.

11.     Drake, T.; Ji, P.; Lin, W. Site Isolation in Metal–Organic Frameworks Enables Novel Transition Metal Catalysis. *Acc. Chem. Res.* **2018**.

12.     Furukawa, H.; Cordova, K. E.; O'Keeffe, M.; Yaghi, O. M. The Chemistry and Applications of Metal-Organic Frameworks. *Science* **2013,** *341* (6149).

13.     Yaghi, O. M.; O'Keeffe, M.; Ockwig, N. W.; Chae, H. K.; Eddaoudi, M.; Kim, J. Reticular synthesis and the design of new materials. *Nature* **2003,** *423*, 705.

14.     Gascon, J.; Corma, A.; Kapteijn, F.; Llabrés i Xamena, F. X. Metal Organic Framework Catalysis: Quo vadis? *ACS Catal.* **2013,** *4* (2), 361-378.

15.     Corma, A.; García, H.; Llabrés i Xamena, F. X. Engineering Metal Organic Frameworks for Heterogeneous Catalysis. *Chem. Rev.* **2010,** *110* (8), 4606-4655.

16.     Wang, C.; Xie, Z.; deKrafft, K. E.; Lin, W. Doping Metal–Organic Frameworks for Water Oxidation, Carbon Dioxide Reduction, and Organic Photocatalysis. *J. Am. Chem. Soc.* **2011,** *133* (34), 13445-13454.

17.     Manna, K.; Zhang, T.; Carboni, M.; Abney, C. W.; Lin, W. Salicylaldimine-Based Metal–Organic Framework Enabling Highly Active Olefin Hydrogenation with Iron and Cobalt Catalysts. *J. Am. Chem. Soc.* **2014,** *136* (38), 13182-13185.

18.     Manna, K.; Zhang, T.; Lin, W. Postsynthetic Metalation of Bipyridyl-Containing Metal–Organic Frameworks for Highly Efficient Catalytic Organic Transformations. *J. Am. Chem. Soc.* **2014,** *136* (18), 6566-6569.

19.     Manna, K.; Zhang, T.; Greene, F. X.; Lin, W. Bipyridine- and Phenanthroline-Based Metal–Organic Frameworks for Highly Efficient and Tandem Catalytic Organic Transformations via Directed C–H Activation. *J. Am. Chem. Soc.* **2015,** *137* (7), 2665-2673.

20.     Cao, L.; Lin, Z.; Peng, F.; Wang, W.; Huang, R.; Wang, C.; Yan, J.; Liang, J.; Zhang, Z.; Zhang, T.; Long, L.; Sun, J.; Lin, W. Self-Supporting Metal–Organic Layers as Single-Site Solid Catalysts. *Angew. Chem. Int. Ed.* **2016,** *55* (16), 4962-4966.

21.     Øien, S.; Agostini, G.; Svelle, S.; Borfecchia, E.; Lomachenko, K. A.; Mino, L.; Gallo, E.; Bordiga, S.; Olsbye, U.; Lillerud, K. P.; Lamberti, C. Probing Reactive Platinum Sites in UiO-67 Zirconium Metal–Organic Frameworks. *Chem. Mater.* **2015,** *27* (3), 1042-1056.

22.     Fang, X.; Shang, Q.; Wang, Y.; Jiao, L.; Yao, T.; Li, Y.; Zhang, Q.; Luo, Y.; Jiang, H.-L. Single Pt Atoms Confined into a Metal–Organic Framework for Efficient Photocatalysis. *Adv. Mater.* **2018,** *30* (7), 1705112.

23.     Copéret, C.; Liao, W.-C.; Gordon, C. P.; Ong, T.-C. Active Sites in Supported Single-Site Catalysts: An NMR Perspective. *J. Am. Chem. Soc.* **2017,** *139* (31), 10588-10596.

24.    DeRita, L.; Dai, S.; Lopez-Zepeda, K.; Pham, N.; Graham, G. W.; Pan, X.; Christopher, P. Catalyst Architecture for Stable Single Atom Dispersion Enables Site-Specific Spectroscopic and Reactivity Measurements of CO Adsorbed to Pt Atoms, Oxidized Pt Clusters, and Metallic Pt Clusters on TiO2. *J. Am. Chem. Soc.* **2017,** *139* (40), 14150-14165.

25.    Ding, K.; Gulec, A.; Johnson, A. M.; Schweitzer, N. M.; Stucky, G. D.; Marks, L. D.; Stair, P. C. Identification of active sites in CO oxidation and water-gas shift over supported Pt catalysts. *Science* **2015,** *350* (6257), 189-192.

26.    Cao, L.; Luo, Q.; Liu, W.; Lin, Y.; Liu, X.; Cao, Y.; Zhang, W.; Wu, Y.; Yang, J.; Yao, T.; Wei, S. Identification of single-atom active sites in carbon-based cobalt catalysts during electrocatalytic hydrogen evolution. *Nat. Catal.* **2019,** *2* (2), 134-141.

27.    Liu, J. Aberration-corrected scanning transmission electron microscopy in single-atom catalysis: Probing the catalytically active centers. *Chin. J. Catal.* **2017,** *38* (9), 1460-1472.

28.    Spezzati, G.; Su, Y.; Hofmann, J. P.; Benavidez, A. D.; DeLaRiva, A. T.; McCabe, J.; Datye, A. K.; Hensen, E. J. M. Atomically Dispersed Pd–O Species on CeO2(111) as Highly Active Sites for Low-Temperature CO Oxidation. *ACS Catal.* **2017,** *7* (10), 6887-6891.

29.    Pennycook, S. J.; Jesson, D. E. High-resolution Z-contrast imaging of crystals. *Ultramicroscopy* **1991,** *37* (1), 14-38.

30.    Jones, J.; Xiong, H.; DeLaRiva, A. T.; Peterson, E. J.; Pham, H.; Challa, S. R.; Qi, G.; Oh, S.; Wiebenga, M. H.; Pereira Hernández, X. I.; Wang, Y.; Datye, A. K. Thermally stable single-atom platinum-on-ceria catalysts via atom trapping. *Science* **2016,** *353* (6295), 150-154.

31.    Nie, L.; Mei, D.; Xiong, H.; Peng, B.; Ren, Z.; Hernandez, X. I. P.; DeLaRiva, A.; Wang, M.; Engelhard, M. H.; Kovarik, L.; Datye, A. K.; Wang, Y. Activation of surface lattice oxygen in single-atom Pt/$CeO_2$ for low-temperature CO oxidation. *Science* **2017,** *358* (6369), 1419-1423.

32.    Therrien, A. J.; Hensley, A. J. R.; Marcinkowski, M. D.; Zhang, R.; Lucci, F. R.; Coughlin, B.; Schilling, A. C.; McEwen, J.-S.; Sykes, E. C. H. An atomic-scale view of single-site Pt catalysis for low-temperature CO oxidation. *Nat. Catal.* **2018,** *1* (3), 192-198.

33.     Liu, J.; Lucci, F. R.; Yang, M.; Lee, S.; Marcinkowski, M. D.; Therrien, A. J.; Williams, C. T.; Sykes, E. C. H.; Flytzani-Stephanopoulos, M. Tackling CO Poisoning with Single-Atom Alloy Catalysts. *J. Am. Chem. Soc.* **2016,** *138* (20), 6396-6399.

34.     Marcinkowski, M. D.; Jewell, A. D.; Stamatakis, M.; Boucher, M. B.; Lewis, E. A.; Murphy, C. J.; Kyriakou, G.; Sykes, E. C. H. Controlling a spillover pathway with the molecular cork effect. *Nat. Mater.* **2013,** *12*, 523.

35.     Marcinkowski, M. D.; Darby, M. T.; Liu, J.; Wimble, J. M.; Lucci, F. R.; Lee, S.; Michaelides, A.; Flytzani-Stephanopoulos, M.; Stamatakis, M.; Sykes, E. C. H. Pt/Cu single-atom alloys as coke-resistant catalysts for efficient C–H activation. *Nature Chem.* **2018,** *10*, 325.

36.     Li, X.; Bi, W.; Zhang, L.; Tao, S.; Chu, W.; Zhang, Q.; Luo, Y.; Wu, C.; Xie, Y. Single-Atom Pt as Co-Catalyst for Enhanced Photocatalytic H2 Evolution. *Adv. Mater.* **2016,** *28* (12), 2427-2431.

37.     Cheng, N.; Stambula, S.; Wang, D.; Banis, M. N.; Liu, J.; Riese, A.; Xiao, B.; Li, R.; Sham, T.-K.; Liu, L.-M.; Botton, G. A.; Sun, X. Platinum single-atom and cluster catalysis of the hydrogen evolution reaction. *Nature Communications* **2016,** *7*, 13638.

38.     Wei, H.; Huang, K.; Wang, D.; Zhang, R.; Ge, B.; Ma, J.; Wen, B.; Zhang, S.; Li, Q.; Lei, M.; Zhang, C.; Irawan, J.; Liu, L.-M.; Wu, H. Iced photochemical reduction to synthesize atomically dispersed metals by suppressing nanocrystal growth. *Nature Communications* **2017,** *8* (1), 1490.

39.     Li, T.; Liu, J.; Song, Y.; Wang, F. Photochemical Solid-Phase Synthesis of Platinum Single Atoms on Nitrogen-Doped Carbon with High Loading as Bifunctional Catalysts for Hydrogen Evolution and Oxygen Reduction Reactions. *ACS Catal.* **2018,** *8* (9), 8450-8458.

40.     Fuente, E.; Menéndez, J. A.; Díez, M. A.; Suárez, D.; Montes-Morán, M. A. Infrared Spectroscopy of Carbon Materials:  A Quantum Chemical Study of Model Compounds. *The Journal of Physical Chemistry B* **2003,** *107* (26), 6350-6359.

41.     Bloch, E. D.; Britt, D.; Lee, C.; Doonan, C. J.; Uribe-Romo, F. J.; Furukawa, H.; Long, J. R.; Yaghi, O. M. Metal Insertion in a Microporous Metal−Organic Framework Lined with 2,2′-Bipyridine. *J. Am. Chem. Soc.* **2010,** *132* (41), 14382-14384.

42.     Kim, I. S.; Li, Z.; Zheng, J.; Platero-Prats, A. E.; Mavrandonakis, A.; Pellizzeri, S.; Ferrandon, M.; Vjunov, A.; Gallington, L. C.; Webber, T. E.; Vermeulen, N. A.; Penn, R. L.;

Getman, R. B.; Cramer, C. J.; Chapman, K. W.; Camaioni, D. M.; Fulton, J. L.; Lercher, J. A.; Farha, O. K.; Hupp, J. T.; Martinson, A. B. F. Sinter-Resistant Platinum Catalyst Supported by Metal–Organic Framework. *Angew. Chem. Int. Ed.*, n/a-n/a.

43.     Chakarova, K.; Mihaylov, M.; Hadjiivanov, K. FTIR spectroscopic study of CO adsorption on Pt–H–ZSM-5. *Microporous Mesoporous Mater.* **2005,** *81* (1), 305-312.

44.     Uson, R.; Fornies, J.; Tomas, M.; Menjon, B. Synthesis and reactivity of cis and trans dicarbonyl derivatives of platinum(II). *Organometallics* **1986,** *5* (8), 1581-1584.

45.     Kwon, Y.; Kim, T. Y.; Kwon, G.; Yi, J.; Lee, H. Selective Activation of Methane on Single-Atom Catalyst of Rhodium Dispersed on Zirconia for Direct Conversion. *J. Am. Chem. Soc.* **2017,** *139* (48), 17694-17699.

46.     Varshavsky, J. S.; Kiseleva, N. V.; Cherkasova, T. G.; Buzina, N. A. Dimethylformamide carbonylation of platinum group metals under mild homogeneous conditions. Reactions of carbonyl-containing complexes. *J. Organomet. Chem.* **1971,** *31* (1), 119-122.

47.     Zucca, A.; Petretto, G. L.; Stoccoro, S.; Cinellu, M. A.; Manassero, M.; Manassero, C.; Minghetti, G. Cyclometalation of 2,2′-Bipyridine. Mono- and Dinuclear C,N Platinum(II) Derivatives. *Organometallics* **2009,** *28* (7), 2150-2159.

48.     Crabtree, R. H. *The Organometallic Chemistry of the Transition Metals*. Wiley: Hoboken, New Jersey, 2014; Vol. Sixth edition.

49.     Taylor, K. C. Nitric Oxide Catalysis in Automotive Exhaust Systems. *Catalysis Reviews* **1993,** *35* (4), 457-481.

# CHAPTER 5.   GENERAL CONCLUSION

In this thesis, metal-organic frameworks have been shown to be a promising platform for application in heterogeneous catalysis. In chapter 2, we discussed the used of bidentate dicarboxylate organic linker with various functionalities to create the multi-variate metal-organic frameworks. The used differentiate organic functional groups to serve two-fold in modifying the catalytic properties of the metal-organic framework for application in the visible light photooxidation of benzyl alcohol to benzaldehyde. The organic linker allows the tuning of the band gap of the zirconium oxo-cluster active sites, and the pore environment for substrate diffusion. In chapter 3, we further utilized the amino-functionalized linker in the metal-organic framework to stabilized ultrafine Platinum nanoclusters, that can be used as a precursor to synthesize bimetallic nanocluster such as Pt-Sn. The encapsulated Pt-Sn nanocluster has shown promising chemoselectivity for hydrogenation of furfural to furfuryl alcohol. The uniform and monodispersed Pt-Sn nanocluster allow us to use surface sensitive techniques such as DRIFTS-CO to characterize the nanocluster surface. In chapter 4, we apply the surface sensitive techniques of DRIFTS-CO to study the isolated Platinum active sites supported in a bipyridine metal-organic framework. In a nutshell, we were able to apply in-situ IR spectroscopy techniques to probe the isolated Pt structure, which allows us to further understand the structure-property relationship of this single-site catalyst. We anticipate these studies will contribute to the fundamental understanding of catalytic structure at the atomic level, thus allowing us to design better catalyst for a broader applications.